

COMPLETE INTERNAL PHOTON DOSIMETRY CHARACTERIZATION  
OF THE UNIVERSITY OF FLORIDA  
NEWBORN HYBRID COMPUTATIONAL DOSIMETRY PHANTOMS

By

MICHAEL B. WAYSON

A THESIS PRESENTED TO THE GRADUATE SCHOOL  
OF THE UNIVERSITY OF FLORIDA IN PARTIAL FULFILLMENT  
OF THE REQUIREMENTS FOR THE DEGREE OF  
MASTER OF SCIENCE

UNIVERSITY OF FLORIDA

2009

© 2009 Michael B. Wayson

To my family, who has always encouraged my desire for higher education. To my beautiful fiancée, for whom this work is but one more step towards our wonderful life together. To my Lord and Savior Jesus Christ, without whom I would not be in the position that I am.

## ACKNOWLEDGMENTS

I thank Dr. Wesley Bolch for his guidance, direction, and input, Dr. David Hintenlang for his critiques and input, Dr. Choonsik Lee for his immense technical support for MCNPX, and Arthur Adkins for troubleshooting my many issues with the Advanced Laboratory for Radiation Dosimetry Studies (ALRADS) computer cluster. I thank my family and my fiancée, Leslie, for their continual support and encouragement. Finally, I thank God for blessing me with the opportunity and ability to pursue a rewarding career.

## TABLE OF CONTENTS

	<u>Page</u>
ACKNOWLEDGMENTS .....	4
LIST OF TABLES .....	7
LIST OF FIGURES .....	8
LIST OF ABBREVIATIONS.....	9
ABSTRACT.....	11
CHAPTER	
1 INTRODUCTION .....	13
Background.....	13
History of Computational Dosimetry Phantoms.....	15
Purpose of Study.....	19
2 MATERIALS AND METHODS .....	24
UF Newborn Hybrid Dosimetry Phantom.....	24
Subsegmented Skeleton Development .....	26
Skeletal Photon Dose Response Functions.....	28
Computational Dosimetry Simulations.....	31
Internal Dosimetry Formulation .....	36
Renal Function Case Study.....	39
Clinical Aspects.....	39
Dosimetry Assessment .....	40
Biokinetics.....	40
Whole-body effective dose.....	41
3 RESULTS.....	49
Skeletal Dose Response Functions .....	49
Specific Absorbed Fractions.....	51
Renal Function Case Study.....	51
4 DISCUSSION.....	59
ORNL Dose Response Functions .....	59
ORNL Newborn Specific Absorbed Fractions .....	60
Renal Function Case Study.....	61
5 CONCLUSION.....	67

APPENDIX

A	SAMPLE FILES .....	69
B	ORIGINAL CODES .....	96
	LIST OF REFERENCES .....	104
	BIOGRAPHICAL SKETCH .....	107

## LIST OF TABLES

<u>Table</u>		<u>Page</u>
2-1	Active marrow distribution comparison .....	43
2-2	Mineral bone distribution in the UF newborn hybrid phantoms.....	44
2-3	Source organs for the male and female UF newborn hybrid phantoms.....	45
2-4	Biokinetic parameters for $^{99m}\text{Tc}$ -DMSA for the newborn patient .....	45
3-1	Specific absorbed fractions for the liver source in the female UF newborn hybrid phantom.....	53
3-2	Source organ residence times for $^{99m}\text{Tc}$ -DMSA in a newborn .....	55
3-3	Internal dosimetry results and tissue weighting factors for the renal function case study.....	55
4-1	Newborn skeletal dose response function comparison. ....	63
4-2	Newborn specific absorbed fraction comparison.....	64
4-3	Renal function dosimetry comparison .....	65

## LIST OF FIGURES

<u>Figure</u>	<u>Page</u>
1-1 The first stylized model of the trunk of an adult human.....	21
1-2 The MIRDP Pamphlet No. 5 revised stylized computational dosimetry phantom.....	22
1-3 The complete current ORNL stylized computational dosimetry phantoms.....	22
1-4 The VIP-Man voxel phantom .....	23
1-5 A representative set of voxel phantoms for the GSF family of voxel phantoms.....	23
2-1 Coronal and sagittal views of the UF newborn voxel computational dosimetry phantom.....	46
2-2 Steps in the process of converting the original newborn voxel model into a NURBS model and voxelizing for input into MCNPX.....	47
2-3 The UF newborn hybrid female phantom in NURBS format.....	47
2-4 Sample bone sites of the UF newborn hybrid phantom heterogeneous skeleton. ....	48
2-5 Voxelized UF newborn hybrid female phantom.....	48
3-1 Dose and kerma response functions.....	56
3-2 Skeletal dose response functions for all bone sites.....	57
3-3 Specific absorbed fractions from the liver source in the female UF newborn hybrid phantom.....	58
4-1 UF newborn hybrid phantom and ORNL adult male stylized phantom photon dose response functions.....	66

## LIST OF ABBREVIATIONS

AF	absorbed fraction
ALRADS	Advanced Laboratory for Radiation Dosimetry Studies
AM	active marrow
CB	cortical bone
CPE	charged particle equilibrium
CT	computed tomography
DMSA	dimercaptosuccinic acid
DRF	dose response function
EGSnrc	Electron-Gamma-Shower National Research Council
ICRP	International Commission on Radiological Protection
IDL	Interactive Data Language
KERMA	kinetic energy released per unit mass
MATLAB <sup>TM</sup>	matrix laboratory
MCNP5	Monte Carlo n-particle version 5
MCNPX	Monte Carlo n-particle extended
MIRD	Medical Internal Radiation Dose
NURBS	non-uniform rational b-splines
OLINDA	organ level internal dose assessment
ORNL	Oak Ridge National Laboratory
PET	positron emission tomography
PIRT	paired-image radiation transport
RST	residual soft tissue
SAF	specific absorbed fraction
SNM	Society of Nuclear Medicine

SPECT	single photon emission tomography
TB	trabecular bone
TLD	thermoluminescent dosimeter
TM <sub>50</sub>	bone endosteum
UF	University of Florida

Abstract of Thesis Presented to the Graduate School  
of the University of Florida in Partial Fulfillment of the  
Requirements for the Degree of Master of Science

COMPLETE INTERNAL PHOTON DOSIMETRY CHARACTERIZATION  
OF THE UNIVERSITY OF FLORIDA  
NEWBORN HYBRID COMPUTATIONAL DOSIMETRY PHANTOMS

By

Michael B. Wayson

December 2009

Chair: Wesley Bolch  
Major: Nuclear Engineering Sciences

A very important aspect of nuclear medicine imaging that is always in need of improvement is organ dosimetry. Since nuclear medicine imaging is based on the biodistribution of an administered radiopharmaceutical, radiation is emitted from the set of organs to which the radiopharmaceutical localizes. The determination of tissue absorbed dose from radiations emitted from inside the human body is known as internal dosimetry and is an integral part of performing risk assessment for nuclear medicine imaging. Computational radiation dosimetry is typically performed for such procedures owing to the difficulties of using physical phantoms and dose measuring devices for organ dose assessment.

This study discusses the recent advancements in computational dosimetry methods, develops an improved method of determining dose to the human skeleton from incident photons, and calculates a new comprehensive set of photon specific absorbed fractions for the University of Florida newborn hybrid phantoms for use in internal dosimetry estimates. The set of specific absorbed fractions can be used to calculate the effective dose for any nuclear medicine imaging procedure, provided the radiopharmaceutical biokinetics and radionuclide decay information are known.

Accurate dosimetry is needed in nuclear medicine imaging for the purpose of reducing patient risk and developing secondary cancer risk models. The results of this study provide the latest improvement in photon specific absorbed fractions and will be extended to the complete University of Florida hybrid computational phantom series in the future.

## CHAPTER 1 INTRODUCTION

“Our goal is to ensure that all children receive safe, quality care when they undergo medical imaging examinations” (1). This statement was made by Marilyn Goske, M.D., chair of the Alliance for Radiation Safety in Pediatric Imaging in a press release honoring the Alliance for their Image Gently campaign initiative. The Alliance was founded by the Society for Pediatric Radiology, the American Society of Radiologic Technologists, the American College of Radiology, and the American Association of Physicists in Medicine. The Image Gently campaign was created to educate radiologic technologists, medical physicists, radiologists, pediatricians, and parents about the radiation dose to children during computed tomography (CT) exams (1). Recently, the Alliance has created a new campaign that emphasizes radiation dose considerations during fluoroscopic procedures called Step Lightly (2). It has been shown that children are at a higher risk of expressing radiation induced effects later in life than adults from medical procedures involving radiation (3). This is explained by the fact that children are inherently more sensitive to radiation because their bodies are still developing along with the fact that children have a much longer time to express radiation induced effects. These observations lead to the conclusion of great importance that radiation dose to children must be minimized for any given medical diagnostic procedure. While the Image Gently and Step Lightly campaigns emphasize minimizing radiation dose in CT and fluoroscopic imaging, they underscore the fact that radiation dose must be minimized for *any* medical procedure that involves ionizing radiation, including the imaging method of emphasis in this study: nuclear medicine.

### **Background**

Occupational dosimetry in the clinical environment is typically assessed by way of physical dosimeters. Usually, thermoluminescent dosimeters (TLDs) are used to record an

integral dose for medical workers whose duties include working with radiation. The TLDs are then analyzed and the integral radiation dose is recorded for that worker. While this works well for determining occupational exposures, the patient undergoing a medical procedure involving radiation does not receive a physical dosimeter to determine the absorbed dose to the patient. This is due in large part to the difficult logistics and cost of individually analyzing TLDs for every patient for every exam, which is simply impractical. Because of the logistical difficulty of utilizing physical dosimeters for everyday medical dosimetry, methods of determining patient dose have been investigated extensively over the years. Accurately calculating radiation dose to a patient is an important and generally missing step in the medical examination of the patient.

Quantifying radiation dose is essential for the purpose of assessing risk of effects resulting from radiation exposure. Studies performed on the Japanese atomic bomb survivors showed that an increase in radiation exposure led to an increase in excess cancer mortality for the study population (4). The result of that study made it clear that excessive exposure to radiation is detrimental to the human body. While comprehensive studies of cancer risk associated with low doses of radiation have not been conducted thus far, the mechanisms for increased cancer risk from *any* exposure to radiation can be explained.

As a basic example, the mechanism for increased cancer risk from the absorption of electromagnetic radiation (photon) will be explained. The incident photon interacts with molecules within a cell in human tissue. Through either photoelectric or Compton scattering interactions, an electron is liberated by the photon. This forms a free radical which is an atom or molecule that possesses an unpaired orbital electron in the outer shell (4). For example, an interaction with a water molecule could produce the reaction  $\text{H}_2\text{O} \rightarrow \text{H}_2\text{O}^+ + \text{e}^-$ , where the water molecule is ionized and an electron is liberated. The water ion radical then interacts with a

second water molecule, producing the reaction  $\text{H}_2\text{O}^+ + \text{H}_2\text{O} \rightarrow \text{H}_3\text{O}^+ + \text{OH}\cdot$ , where  $\text{OH}\cdot$  is a highly reactive product known as the hydroxyl radical (4). The hydroxyl radical then interacts with DNA to create a DNA radical which can lead to DNA strand breaks. If the strand breaks are not repaired, DNA mutation can occur and lead to the genesis of cancer. This is one example of how incident radiation, in this case, photons, may lead to cancer. It would follow, then, that any incident radiation is cause for concern.

The pertinent application to medical imaging is that one must always attempt to minimize the radiation dose to the patient. Obviously, medical imaging aims to procure an accurate diagnosis, so image quality is also a priority when administering an exam. There is a constant balance between radiation dose and image quality that medical professionals must always keep in mind when examining their patients, but this is not always possible due to insufficient quantitative relationships between radiation dose and image quality. This optimization may only become a reality when the dosimetry performed for medical imaging is as accurate as possible.

### **History of Computational Dosimetry Phantoms**

As previously discussed, physical dosimeters are not used for patients undergoing medical imaging procedures involving radiation. Therefore, a different method of determining radiation dose was developed. This method involved the use of computational dosimetry phantoms. Computational dosimetry phantoms are virtual representations of humans which are then input into radiation transport codes to calculate radiation dose from any defined radiation source. This is contrast to another type of dosimetry phantom: a physical dosimetry phantom. These are physical constructs made to model human anatomy, based on CT data, which are then integrated with physical dosimeters. It is not always optimal to utilize physical dosimetry phantoms because they cannot be easily modified once built.

The computational dosimetry phantoms may be used to assess the absorbed radiation dose from a variety of radiation sources. Medical imaging radiation sources include external radiation beams employed in modalities such as general radiography, CT, or fluoroscopy or internal sources such as nuclear medicine imaging modalities which encompasses positron emission tomography (PET) and single photon emission computed tomography (SPECT). The emphasis of this study was the analysis of internal sources.

An early attempt at creating a virtual representation of humans was described in the Society of Nuclear Medicine's (SNM) Medical Internal Radiation Dose (MIRD) committee pamphlet No. 3 in 1968. The MIRD committee tabulated a set of photon absorbed fractions (AF) for an adult phantom which was comprised of a combination of simple mathematical shapes such as spheres, ellipsoids, and elliptical and right circular cylinders (5). Tissues of the human body were homogeneous in nature and included elements H, C, N, O, Cl, and Na (5). Computational dosimetry phantoms made up of simple mathematical shapes are referred to as stylized phantoms.

Another early model was developed by Oak Ridge National Laboratory (ORNL) in the early 1960s and was a whole body model created for the purpose of external beam dosimetry (6). This model attempted to represent the trunk of an adult and was a simple right circular cylinder 30 cm in diameter and 60 cm in height. This early generation phantom can be seen in Figure 1-1.

In the mid-1960s, ORNL developed a new stylized adult phantom called the Fisher-Snyder Phantom. This model consisted of three distinct regions: the head and neck, the trunk including arms, and the legs. The head and neck were described by an elliptical cylinder, the trunk and arms also by an elliptical cylinder, and the legs by truncated elliptical cones (7). Some structures

left out of this model include hands, feet, ears, nose, lungs, or skeleton. All tissues were assumed to be homogeneous.

The MIRDC committee published in 1969 an advancement of the Fisher-Snyder adult phantom in their 5<sup>th</sup> pamphlet. The Fisher-Snyder phantom was a *heterogeneous* model of the adult and was officially called the MIRDC Phantom (7). In this phantom, 22 internal organs were modeled by way of three dimensional surface equations. Three body tissues were modeled: skeletal tissue, lung tissue, and soft tissue. Photon AFs were calculated for 12 energies with a range of 25,000 to 50,000 histories for each calculation (7). The MIRDC Phantom was later revised in 1978 with improvements in the organ models and statistics. The number of photon histories was increased to 60,000 for each source organ (8). The revised MIRDC 5 adult phantom can be seen in Figure 1-2.

Development of pediatric models also took place in the 1970s at ORNL. Early attempts at pediatric models involved the simple down-scaling of the adult MIRDC Phantom. A newborn phantom along with 1-yr, 5-yr, 10-yr, and 15-yr phantoms were created in this fashion.

Currently, the international standard for computational dosimetry phantoms is the phantom model series created in 1980 by Mark Cristy and Keith Eckerman. These phantoms were a revision to the ORNL pediatric series of models and can be seen in Figure 1-3. The key improvements of these models were new models of the heart, breasts, and thyroid and a new model for skeletal dosimetry using dose-response functions (DRFs) (9). A complete set of specific absorbed fractions (SAF) were calculated for each of these phantoms.

All of the previously described phantoms are stylized phantoms. That is, they are described by mathematical shapes. While this method of representing humans for the purpose of computational dosimetry is flexible and easy to use, it is not very anatomically realistic. A more

anatomically realistic way of representing humans is to use actual anatomic data to create a computational phantom. This is done by using medical images of actual patients to create phantoms. For example, a CT image set of a patient may be segmented to yield almost an exact copy of the patient who was scanned. This data is then voxelized for use in radiation transport codes. The term voxelization refers to the process of transforming a shape or combination of shapes into an equivalent conglomerate of rectangular prisms. Frequently, the rectangular prisms are defined to have equal length sides, thereby forming a set of cubes. If these cubes are created at a fine enough resolution, the original shape can be faithfully represented.

The phantoms created from original image sets were very anatomically realistic, but they were unable to be extended to a variety of applications due to their specific nature. A phantom created from a specific patient's image set can only be accurately used for dosimetry on that patient because it is very difficult to adjust the size and position of a voxel phantom. Since the process of segmentation is so tedious, individual voxel phantoms cannot be created for every patient who undergoes a medical image exam. In addition, some structures in the body such as the large and small intestines are virtually impossible to accurately segment on a CT or magnetic resonance (MR) image.

One previous voxel phantom was the VIP-Man, created using transverse color photographic images from the National Library of Medicine's Visible Human Project (10). The subject was a recently executed 38 year old male from Texas. The resulting voxel model can be seen in Figure 1-4. Another example of previous voxel phantoms is the GSF voxel phantom family (11). This set of phantoms includes females of 8 weeks, 7 years, 26 years, and 40 years, males of 38 years, a second 38 year old, 48 years, and an unknown age, two physical phantoms

representing a torso and head and the thorax, and one female standardized gastrointestinal tract. A representative set of this family of voxel phantoms can be seen in Figure 1-5.

So, while voxel phantoms are preferred in terms of anatomic realism, they lack in flexibility of use. The reverse is true for stylized phantoms. The drawbacks of these respective options for computational radiation dosimetry necessitate a bridge between the stylized and voxel phantoms which would allow for anatomic realism as well as flexibility of use. This study addresses that void and describes the recent advancement in computational dosimetry phantoms: hybrid dosimetry phantoms.

### **Purpose of Study**

It is clear from the previous discussion that there is a need for accurate radiation dosimetry for patients undergoing medical imaging procedures involving radiation. This study addresses the advancements in computer modeling of humans that have been made at the University of Florida (UF) and the current state of computation dosimetry phantoms. The study then presents a DRF model which potentially greatly improves the state of skeletal dosimetry. Finally, a complete dosimetry characterization of the current UF newborn hybrid phantom will be presented. The dosimetry characterization entails a presentation of a complete set of photon SAFs for application to internal dosimetry. These SAFs are paramount in accurately calculating absorbed dose to tissues of interest for any given nuclear medicine procedure. The resultant absorbed doses to tissues of interest can then be used to calculate an effective whole body dose. The SAFs may also be extended to any situation where a human has either inhaled or ingested photon emitting radionuclides. Eventually, the SAFs from this study will be incorporated into a computer program which will allow the user to quickly and accurately assess the effective dose to any newborn patient undergoing a nuclear medicine procedure. This is one step in a line of many that will establish a new SAF dataset to be used for *any* patient from a newborn to an adult.

The determination of dose for actual patients undergoing nuclear medicine procedures is useful for dose tracking and the eventual determination of radiation risk, but another application of dosimetry characterization involves the use of computational phantoms alone. Employing computational phantoms is an effective and safe way of optimizing diagnostic procedures. Injecting a particular patient with varying amounts of radiopharmaceutical for PET imaging and measuring the subsequent image quality is not a safe way of optimizing the procedure. Instead, virtual patients would be used, thus sparing the dose to the patient.

The application of the results of this study is very powerful and will provide insight into the safest way to image patients. A typical procedure performed on newborn patients was explored in this study and will be presented. A whole body dose estimate was calculated for a renal function imaging procedure to demonstrate the ease and accuracy of application.

One example of an application of the data resulting from this study shows that dosimetry can be performed for any nuclear medicine imaging procedure. There is much work to be done to extend this analysis to the whole family of UF hybrid phantoms for both photon and electron dosimetry, but a comprehensive set of photon SAFs for the UF newborn hybrid phantom is a big step in the right direction.

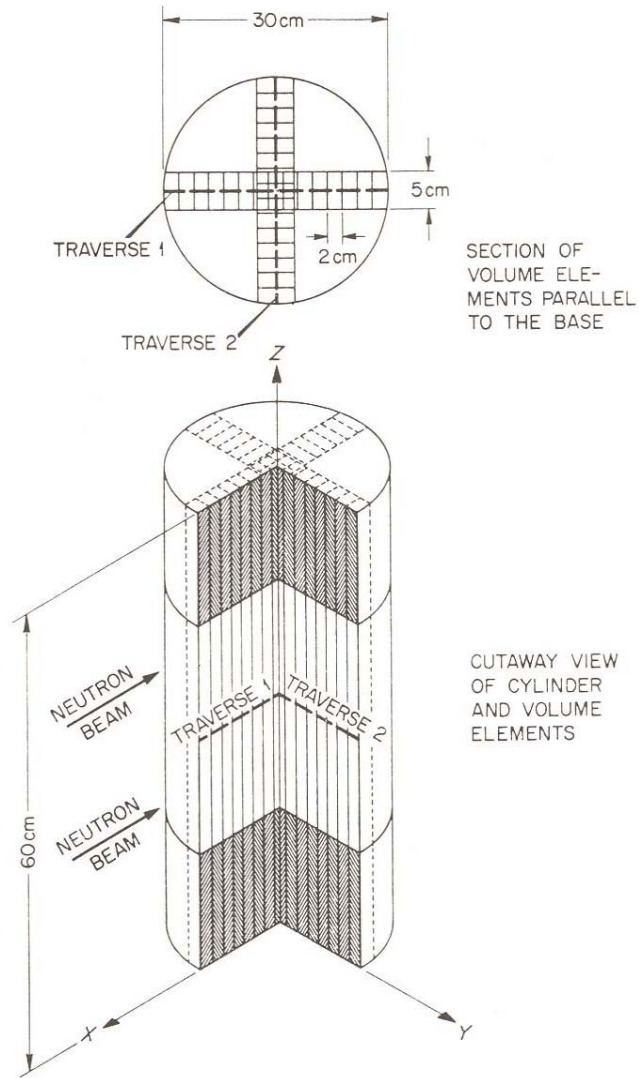


Figure 1-1. The first stylized model of the trunk of an adult human. A right circular cylinder 30 cm in diameter and 60 cm in height (6).

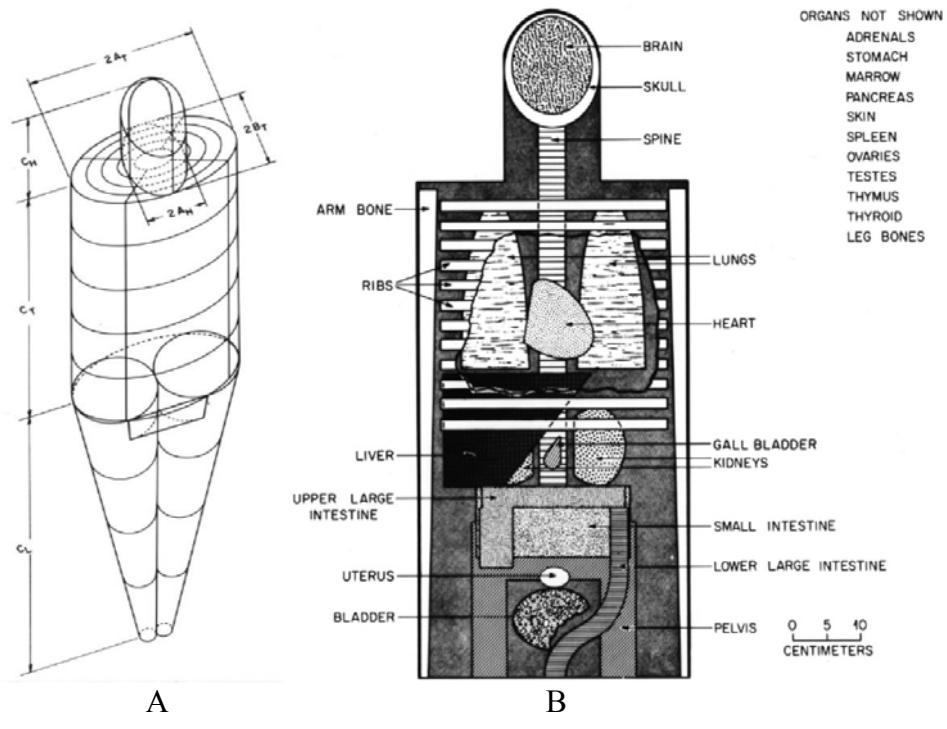


Figure 1-2. The MIRP Pamphlet No. 5 revised stylized computational dosimetry phantom (9).  
 A) Outer body contour. B) Anterior view of principle organs in head and trunk.

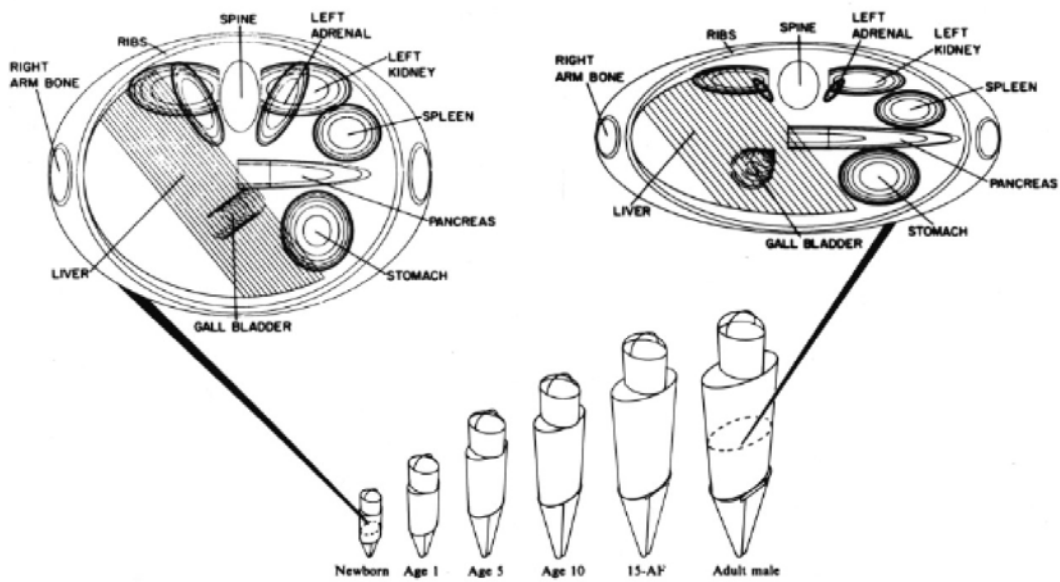


Figure 1-3. The complete current ORNL stylized computational dosimetry phantom series (9).

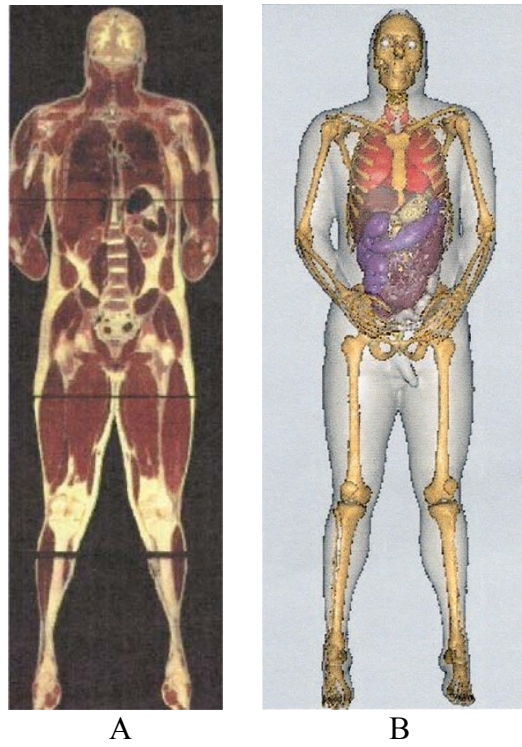


Figure 1-4. The VIP-Man voxel phantom (10). A) Original image used for segmentation. B) Final VIP-Man voxel model.

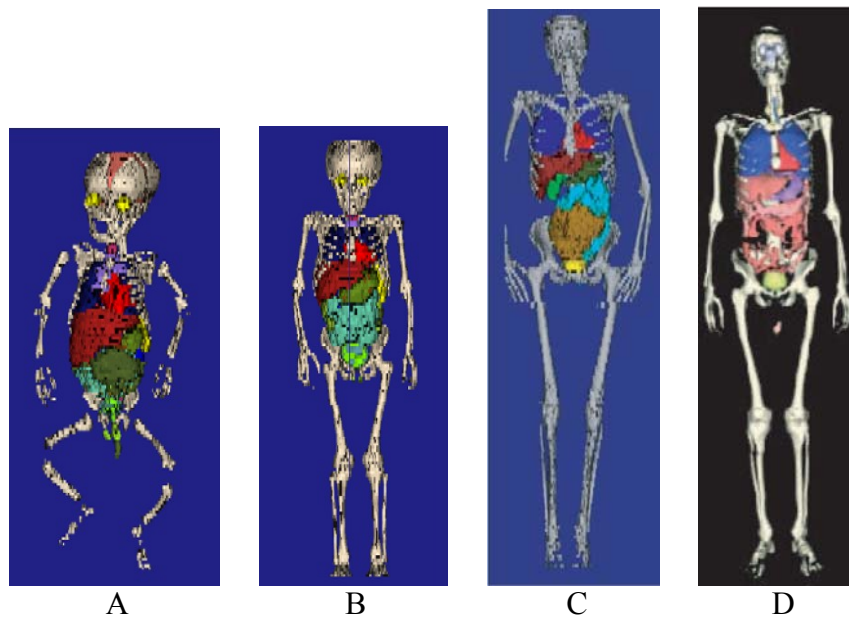


Figure 1-5. A representative set of voxel phantoms for the GSF family of voxel phantoms (11). A) Baby. B) Child. C) Adult female - Donna. D) Adult male - Golem.

## CHAPTER 2 MATERIALS AND METHODS

### **UF Newborn Hybrid Dosimetry Phantom**

The computational dosimetry phantoms discussed previously represent the 1<sup>st</sup> and 2<sup>nd</sup> generation phantoms. The simple stylized phantoms based on mathematical functions were the 1<sup>st</sup> generation phantoms. The medical image-based voxel phantoms were the 2<sup>nd</sup> generation phantoms. A 3<sup>rd</sup> generation phantom has recently emerged and has been progressed extensively at UF. This 3<sup>rd</sup> generation phantom combines the concepts of the 1<sup>st</sup> and 2<sup>nd</sup> generation phantoms to yield a new phantom which possesses both anatomical realism and flexibility of modification.

A mathematical modeling technique commonly used for computer animation is called non-rational b-spline (NURBS) surfaces. NURBS surfaces can model virtually any free-form shape, so they are very useful in modeling complicated volumes such as those found in the human body. They are both flexible and easily modifiable. Because of this, NURBS technology was selected as the primary tool to create a new generation of phantoms that display both anatomic realism and flexibility of use. Since this 3<sup>rd</sup> generation phantom is a sort of mix between stylized and voxel phantoms (as will be seen later), the 3<sup>rd</sup> generation phantom has been termed a “hybrid” phantom.

The UF newborn hybrid phantom is an advancement of the previous UF newborn voxel phantom (12). The voxel model of the newborn was constructed from a CT scan of a 6 day old female (13). This scan was saved as a 512 x 512 x 485 data array with a slice thickness of 1 mm. At this slice thickness and data array size, the UF newborn voxel model was the highest resolution model at the time (13). Delineation of organs was then performed using an in-house Interactive Data Language (IDL) (ITT Visualization Solutions, Boulder, CO) code, and 66

different anatomic regions were defined (13). The UF newborn voxel model can be seen in Figure 2-1.

The software *3D-DOCTOR*<sup>TM</sup> (Able Software Corp., Lexington, MA) was used to convert the UF newborn voxel phantom into a polygon mesh geometry. The voxel phantom was imported into *3D-DOCTOR*, and individual organs were segmented using interactive segmentation tools (12). Once all organs of interest were segmented, the polygon mesh model was imported to *Rhinoceros*<sup>TM</sup> (McNeel North America, Seattle, WA), a NURBS modeling software, to transform the polygon mesh geometry into a NURBS geometry. Seven distinct anatomic groups were defined and imported separately into *Rhinoceros*: the exterior body contour, the respiratory system, the alimentary system, the circulatory system, the urogenital system, other soft tissue organs, and the skeleton (12). The organs of interest were then converted to NURBS surfaces. A NURBS surface is much easier to manipulate than a polygon mesh volume because NURBS surfaces are defined by a series of control points which can be individually manipulated in three dimensions. Volumes bounded by NURBS surfaces can easily be scaled in one, two, or three dimensions. In view of this, it was desired that as many organs as possible be modeled using NURBS surfaces.

Conversion from a polygon mesh geometry originating from manual segmentation to a NURBS geometry was relatively simple, but several small organs and organs that were difficult to segment from the original CT data had to be defined in a different way. Small organs such as the eyes, lenses, ovaries, urinary bladder, breasts, pituitary gland, and tonsils were modeled using stylistic NURBS-based models (12). The original shapes and positions of these organs were referenced from the CT data and faithfully followed in the construction of stylistic representative shapes. The contents of walled organs such as the heart, gall bladder, and urinary bladder were

modeled by copying the organ wall and scaling inward (12). The esophagus, small intestine, colon, and rectum were unable to be segmented from the original CT data, so a three dimensional trace of the lumen centroid was approximated from the segmented UF newborn voxel phantom (12). This was not feasible for the small intestine due to CT slice discontinuity, so a stylistic model was created and approved by a pediatric radiologist (12).

At this point, a newborn hybrid computational dosimetry phantom was completed, but the model represented the patient from which the original CT data was obtained. This patient was not necessarily representative of the 50<sup>th</sup> percentile newborn. Therefore, the International Commission on Radiological Protection's (ICRP) Publication 89 was utilized to adjust the UF newborn hybrid phantom to reflect a 50<sup>th</sup> percentile newborn (12). Once the finalized UF newborn hybrid phantom was created, it was voxelized for use in a radiation transport code, as will be discussed later. The process of taking the original UF newborn voxel phantom, processing it with the previous discussed methods, and voxelizing it for use in a radiation transport code can be seen in Figure 2-2. The completed UF hybrid newborn female phantom can be seen in Figure 2-3.

### **Subsegmented Skeleton Development**

In the first iteration of the UF newborn hybrid phantom, the skeleton was described by a homogeneous model. The homogeneous skeletal model was taken from the UF newborn voxel model and implemented by the use of a combination of NURBS and polygon mesh geometry. The output of the segmentation process and subsequent input into *Rhinoceros* is inherently in the polygon mesh format. Since many bone sites are unable to be effectively modeled with NURBS surfaces, they are left in the polygon mesh format. However, the ribs were sometimes distorted due to the CT slice thickness, so the ribs were created stylistically by creating pipe shapes based on central tracks taken from the original polygon mesh rib cage model (14). This homogeneous

skeletal model treated all bone sites as a uniform mixture of cortical bone, trabecular bone, active bone marrow, and inactive bone marrow. Considering the anatomical realism of the rest of the hybrid phantom, the skeleton was lacking in detail.

The human skeleton consists of three distinct regions: the cortical bone, spongiosa region, and cartilage regions. The spongiosa region is made up of trabecular bone (TB), active bone marrow (AM), and inactive bone marrow. The newborn, however, only possesses AM (14). To produce accurate skeletal dosimetry, an accurate skeletal model must be used, so the homogeneous skeletal model needed to be updated to include all regions of the human skeleton.

The process of creating a multiple region skeletal model began with the segmentation of all bone sites from a set of whole-body cadaver CT data (14). This was done automatically by adjusting the lower bound of the thresholding window in *3D-DOCTOR* to exclude cartilage (14). Application of this thresholding window allowed for automatic segmentation of the whole skeleton from every CT slice, creating a whole-body homogeneous skeletal model. This initial segmentation provided the outer contour of the skeleton. Next, the cartilage was manually segmented and two distinct cartilage regions were identified: bone-associated cartilage and non-bone-associated cartilage (14).

The spongiosa region and associated sub-regions were then delineated by the analysis of microCT images of selected bone sites (14). The sternum, occipital bone, 2<sup>nd</sup> right rib, 2<sup>nd</sup> left rib, L<sub>2</sub>-L<sub>5</sub> vertebrae, T<sub>9</sub>-T<sub>12</sub> vertebrae, C<sub>3</sub>-C<sub>7</sub> vertebrae, T<sub>1</sub>-T<sub>5</sub> vertebrae, T<sub>10</sub>-T<sub>12</sub> vertebrae, L<sub>1</sub>-L<sub>5</sub> vertebrae, 4<sup>th</sup> right rib, 4<sup>th</sup> left rib, and a portion of the right iliac crest obtained from two specimens were imaged using microCT at an isotropic resolution of 30  $\mu\text{m}$  (14). The AM and TB within each bone site was automatically segmented by visual inspection of the image gradient magnitude (15). This technique separated the AM and TB and created a new binary

image files. These files were then used to calculate the fraction of spongiosa occupied by trabeculae and the fraction occupied by AM. This was performed for every bone site. Skeletal tissue masses were then obtained using methods detailed in Deanna *et al* (14).

A detailed model of the human skeleton including the intricacies of the spongiosa cannot currently be modeled in a NURBS environment and voxelized to a resolution that would preserve the detail of the spongiosa because the microstructure of the spongiosa is too intricate and small in dimension. If a skeletal model including heterogeneous regions of AM and TB were voxelized at a resolution fine enough to preserve the detail of the model, the files created to perform radiation dosimetry would be much too large, and the computer time for the simulations would in turn be extended dramatically. So, while the previously discussed advancements in skeletal tissue modeling for the purpose of computational radiation dosimetry produced extensive data characterizing the distribution of skeletal tissues, the results were not directly applicable to the NURBS phantom. However, the results *did* lay the groundwork for the development of skeletal dosimetry methods that would be incorporated in steps separate from the primary dosimetry simulations. While the AM and TB sub-regions of the spongiosa could not be explicitly modeled in *Rhinoceros*, the spongiosa itself was able to be modeled. So, the final heterogeneous skeletal model was visualized in *Rhinoceros* as a three region model with the regions being the cartilage, cortical bone, and spongiosa. Examples of heterogeneous bone sites in *Rhinoceros* can be seen in Figure 2-4. The orange wireframe regions are cartilage. The black wireframe regions are both cortical bone and spongiosa. Regions of spongiosa are the smaller volume, darker wireframe structures.

### **Skeletal Photon Dose Response Functions**

Since the intricacies of the spongiosa were unable to be explicitly modeled in the NURBS/polygon mesh environment, another technique was used to incorporate the lost

spongiosa detail into the phantom: the skeletal dose response function (DRF). A DRF allows for the pre-calculation of the absorbed dose of a particular region per unit fluence, in this case regions of the skeleton. In other words, separate simulations were performed which were able to model much smaller volumes. The results of these simulations were then used in conjunction with the NURBS-based computational phantom so that the skeletal microstructure did not have to be explicitly modeled in *Rhinoceros*.

First, the radiosensitive cells in skeletal tissue had to be identified. Much research has been done to determine this, and the radiosensitive cells were found to be hematopoietic stem cells, osteoprogenitor cells, and chondrocytes (16). The surrogate tissues for these radiosensitive cells were determined to be AM for hematopoietic stem cells, total shallow marrow otherwise known as endosteum (TM<sub>50</sub>) for osteoprogenitor cells, and unossified cartilage for chondrocytes (16). The endosteal region of the spongiosa was defined as all bone marrow that was within 50  $\mu\text{m}$  of the TB surface (16). For the newborn, only AM is present, so TM<sub>50</sub> and AM<sub>50</sub> are equivalent.

Photons that interact with tissues liberate electrons, and those electrons then directly ionize the medium. The energy deposited in this process, divided by the total mass of the medium irradiated results in the calculated radiation absorbed dose. So, while it is of great interest where the emitted photons are transported, the electrons liberated by those photons must also be taken into account. Because of the small dimensions of the skeletal microstructure, secondary electron transport is a concern. This is due to the fact that electrons liberated by high energy photons have ranges which are relatively large compared to the spacing of the trabeculae in the spongiosa. Accordingly, to properly characterize the behavior of secondary electrons liberated in the skeleton, the AFs for different skeletal source-target combinations were calculated.

The paired-image radiation transport (PIRT) model was used in conjunction with the Electron-Gamma-Shower (EGSnrc) radiation transport code of the National Research Council Canada to calculate the skeletal AFs. The combined model allows for tracking of electrons within the microstructure of the spongiosa as well as the macrostructure of the UF newborn hybrid phantom homogeneous skeletal sites. The microstructure was described with voxels of 60  $\mu\text{m}$  isotropic resolution, and the macrostructure was described with voxels ranging from isotropic resolutions of 50  $\mu\text{m}$  to 200  $\mu\text{m}$  (16). Skeletal AFs were calculated for photons incident on the spongiosa with energies ranging from 1 keV to 10 MeV (16). AM, TB volume, and CB volume were all simulated as source tissues, and AM and TM<sub>50</sub> were simulated as target tissues.

An in-house MATLAB code, *multi\_drf\_fast.m*, was used to calculate the DRFs, based on the AFs of the two target tissues, AM and TM<sub>50</sub>, the elemental compositions of mineral bone (trabecular and cortical), active marrow, and cartilage, and the masses of both source and target regions. The code uses the formulation of the DRF in Equation 2-1 (9):

$$\frac{D(r_T)}{\Psi(E)} = \sum_{r_S} \frac{m_S}{m_T} \sum_i \int_0^\infty \phi(r_T \leftarrow r_S, T_i) (i/\rho)_{r_S} n_{r_S}(T_i) T_i dT_i \quad (2-1)$$

where  $m_S$  and  $m_T$  are the masses of the source and target tissues, respectively,  $\phi(r_T \leftarrow r_S, T_i)$  is the AF in target tissue  $r_T$  from source tissue  $r_S$  for electrons of energy  $T_i$ ,  $(i/\rho)_{r_S}$  are the mass attenuation coefficients for source tissue  $r_S$  where  $i$  represents the photoelectric ( $\tau$ ), Compton ( $\sigma$ ), pair production ( $\kappa$ ), and triplet production ( $\nu$ ) processes,  $n_{r_S}(T_i) T_i dT_i$  is the number of electrons with energies between  $T_i$  and  $T_i + dT_i$  liberated in source tissue  $r_S$  for interaction type  $i$ , and  $D(r_T)/\Psi(E)$  is the DRF relating the absorbed dose to target tissue  $r_T$  to the incident fluence of photons with energy  $E$  on the spongiosa.

“Kinetic energy released per unit mass” (kerma) calculations were also performed using the in-house MATLAB code by setting the AF to one for self-irradiation and to zero for cross fire for every bone site. The kerma approximation assumes that all of the energy of the liberated secondary electrons is locally deposited; none of the energy escapes into any adjacent regions. Thus, for a source region emitting electrons liberated by the incident photons, all of the electrons will be absorbed by that source region, resulting in an AF of approximately one for the irradiation scenario of the source and target regions being the same. Alternately, no electrons emitted from the source region will penetrate adjacent regions, so the AF for the irradiation geometry of the source and target regions not being the same is approximately zero.

### **Computational Dosimetry Simulations**

The tool used for the calculation of the SAFs was Monte Carlo N-Particle eXtended Version 2.5 (MCNPX) which is a radiation transport code developed by Los Alamos National Laboratory and is written in Fortran 90. MCNPX is a three-dimensional, time-dependent computational environment that transports radiation through geometries specified by the user. These geometries can be created by combinations of simple surfaces (planes or cylindrical shells) or macrobodies (cubes, spheres, ellipsoids, etc.). MCNP5 preceded MCNPX and was only able to understand geometries in the context of these simple shapes and surfaces. However, to utilize the complicated geometries of NURBS-based computational dosimetry phantoms, the phantoms had to be broken down into voxel arrays because neither MCNP5 nor MCNPX understand NURBS surfaces. In addition, MCNP5 was unable to understand voxel geometries, so MCNPX was selected as the computation tool. MCNPX is able to stochastically model the transport of radiation through any geometry by way of random number generation. Incoherent and coherent scattering, fluorescent emission after photoelectric absorption, and absorption in electron-positron pair production are all accounted for during photon transport (17). Angular

deflection through multiple scattering events, collisional energy loss, and production of secondary particles are all accounted for during electron and positron transport (17).

Before MCNPX was utilized for radiation transport, a useful geometry was created for MCNPX to read. The computational phantom in its original form is a NURBS-based phantom which can be manipulated in the three-dimensional modelling program *Rhinoceros* as previously discussed. Once the phantom was finalized in *Rhinoceros*, it was exported as a \*.raw (raw triangles) file. An in-house *MATLAB*<sup>TM</sup> (The Mathworks, Inc., Natick, MA) code, *voxelizer6.m*, was used to convert the NURBS model into a voxel model at an isotropic voxel resolution of 0.663 mm, selected based on the reference newborn skin thickness (14). The skin of the phantom is not present in the NURBS format, so an in-house IDL code, *skingenerator.idl*, was used to place skin on the voxel phantom, which is accomplished by adding a layer of voxels on the outer surface of the phantom. Axial, coronal, and sagittal views of the voxelized newborn female phantom can be seen in Figure 2-5.

The binary file output from *skingenerator.idl* was input into a second in-house *MATLAB* code, *GenLattice.m*, which created the \*.lat (lattice) file that MCNPX reads as the radiation transport geometry. The lattice file specifies, in raster style, the organ tag associated with each voxel in the voxel matrix. In this way, MCNPX is able to tally energy deposition or particle fluence in any specified organ in the phantom. At this point, the phantom was ready for use in MCNPX. An excerpt of a lattice file can be seen in Appendix A.

The detailed concept of SAF calculations will be described later, but for the purpose of the MCNPX simulations, it is necessary to understand that SAFs are calculated based on either photons or electrons emitted from a specific organ which are then absorbed in another organ. To accomplish this in MCNPX, source files of the form \*.src were generated using an in-house

Visual Basic code, *lymphcounter.vbp*. The source files specify the voxel coordinates of the source organ as well as the corresponding sampling probability. For most source organs, the sampling probability is set to one, which is indicative of uniform source sampling. Uniform source sampling means that the source is homogeneously distributed throughout the source organ. This is accurate for all organs aside from AM and TB. AM and TB are special cases because detailed microstructure is not able to be created at the selected voxel resolution. As discussed previously, the detailed microstructure was accounted for in the development of the skeletal DRFs. Even though the heterogeneous skeletal model is a vast improvement over the previous homogeneous skeletal model, the spongiosa region of the skeleton is still homogeneous in the phantom that is input into MCNPX. Because of this, if the spongiosa was uniformly sampled to create the AM source, regions of TB would also be sampled and incorrectly included. The same problem would occur if the spongiosa was uniformly sampled to create the TB source. To accurately sample regions of AM from the homogeneous spongiosa model, the bone site-specific source sampling probabilities were adjusted to reflect the AM mass distribution in the skeleton. Specifically, the bone site-specific AM and TB mass fraction was used as the source sampling probability. The same solution was utilized to create the TB source. The AM mass fractions are explicitly shown in Table 2-1 and the TB mass fractions were calculated from bone site-specific TB masses in Table 2-2.

Source files were created for all organs in the male and female newborn phantom, including a total body cartilage source, with the only differing organs being the gender-specific organs. Three other organs that were different between the male and female were the residual soft tissue (RST) and the urinary bladder wall and urinary bladder contents. There was a slight difference in the RST volume due to the difference in volume of the gender-specific organs. The

bladder was also slightly different between the male and female to make room for the gender-specific organs. A complete list of source tissues can be seen in Table 2-3. Target tissues were the same as the source tissue with a few exceptions: cortical and trabecular bone were not targets and bone endosteum was added as a target. At this point, the source file could be successfully read by MCNPX. Excerpts of the liver and AM source files can be seen in Appendix A which demonstrate both uniform and non-uniform sampling probabilities, respectively.

The volumes of every region in the body must be specified for input into MCNPX. Part of the output of *voxelizer6.m* was a complete listing of the number of voxels comprising each organ. The voxel count for each organ was multiplied by the voxel volume of  $(0.663 \text{ cm})^3$  to calculate the volume of each organ. The density of each organ was also specified in the input file. Densities of  $1.02 \text{ g/cm}^3$ ,  $0.572 \text{ g/cm}^3$ ,  $1.65 \text{ g/cm}^3$ ,  $0.0012 \text{ g/cm}^3$ ,  $1.10 \text{ g/cm}^3$ , and  $1.33 \text{ g/cm}^3$  were used for soft tissue, lung tissue, cortical bone, air, cartilage, and spongiosa, respectively (12,14,18). The atomic composition for each of these materials was also specified in the input file and can be seen in Table 3 (14,18). The mass of any organ was calculated by MCNPX based on the volume and density of that organ.

The user must decide what metrics MCNPX must output before the photons are transported. MCNPX utilizes what are called “tallies” to create meaningful output from the code. The tally identifiers important to the determination of SAFs were the F4, F6, and \*F8 tallies. The tallies are specified for every organ that is deemed a target organ. The F4 tally tracks photon flux averaged over the target of interest and is quoted in units of particles/cm<sup>2</sup>. This tally was utilized for determining energy deposition in spongiosa regions of the phantom. The results were used with the skeletal DRFs to calculate the SAF of the total body skeleton. To facilitate this process, the flux across bone sites was tallied in energy bins corresponding to the

energies at which the DRFs were evaluated. The F6 and \*F8 tallies track energy deposition averaged over the target of interest in units of MeV/g and energy deposition over the target of interest in units of MeV, respectively. These tally types were used in non-skeletal targets. The F6 tally assumes that all secondary electrons created by the incident photons are locally deposited. As previously discussed, this is the kerma approximation. This approximation is valid for photon energies that create relatively low energy secondary electrons with short ranges. For high energy photons, secondary electron escape becomes a factor, and the \*F8 tally, which tracks secondary electrons, becomes necessary. \*F8 tallies require more computer time than F6 tallies due to the fact that \*F8 tallies track secondary electrons. This situation affords the ability to increase the number of photons started for F6 tallies, thereby decreasing the uncertainty in the results. A threshold photon energy of 100 keV was chosen as the point at which the F6 tally is abandoned in favor of the \*F8 tally. At this point, the number of photons started was decreased from  $10^8$  to  $10^7$ . This energy threshold was determined by comparing the SAFs of a liver source determined from both F6 and \*F8 tallies at various energies. The difference between the results from the F6 and \*F8 tallies at an energy of 100 keV was found to be ~1 % and was considered acceptable. It is important to note that all tallies are normalized to the number of photons simulated. So, all tally results are inherently in the primary unit of measurement per photon.

There were a total of 61 source organs simulated for the female phantom and a total of 63 source organs simulated for the male phantom at 21 photon energies ranging from 0.01 MeV to 4 MeV for both. From these combinations, 1281 input files were run for the female phantom and 1323 input files for the male phantom for a total of 2604 input files. Due to the number of input files required for a complete dosimetry characterization of both newborn phantoms, a *MATLAB* code, *GenerateInput.m*, was created to automatically generate each input file. The code

generates an input file template that cycles through every photon energy for every source organ and changes the lattice file name, particle importances, simulation mode, tally type, and number of photons started based on the photon energy. If the photon energy is *below* 100 keV, the lattice file name is changed to one which only recognizes photon transport, the photon importance is changed to one and the electron importance is changed to zero because only photons, not secondary electrons, are recognized below 100 keV, the mode is changed to photon transport only, the tally type is switched to F6 as previously discussed, and the number of particles is set to  $10^8$ . If the photon energy is *above* 100 keV, the lattice file name is changed to one which recognizes both photon and secondary electron transport, both the photon and electron importances are set to one because secondary electrons are tracked in addition to photons, the mode is changed to photon and electron transport, the tally type is switched to \*F8 as previously discussed, and the number of particles is set to  $10^7$ . A sample input file for the female newborn phantom at a photon energy of 4 MeV for a liver source can be seen in Appendix A.

The ALRADS computer cluster possesses 56 useable processors, so the large number of input files were able to be divided up and run on many processors. The average computer time for both phantoms was calculated and found to be about 12 hours with a total computer time of about 31248 hours, or 3.6 years. Distributed among many processors, the actual computer time was about 6 weeks. A post-processing *MATLAB* code, *ParseOutput.m*, was written to extract the tallies, convert them to SAFs, and place the results into Microsoft Excel files. This code for the female phantom can be found in Appendix B.

### **Internal Dosimetry Formulation**

The computational dosimetry phantoms were used to calculate a set of SAFs at various photon energies. The SAF is an important measure which reflects the geometry of the irradiation scenario as well as the photon energy. It is ultimately used to calculate either individual organ

absorbed doses, individual organ equivalent doses, or a whole-body effective dose. Dosimetry of internal emitters is derived from the emission of radiation from any source tissue  $r_s$  and the absorption of that radiation in target tissue  $r_T$ . For any target tissue, the time independent formulation of radiation absorbed dose from a set of arbitrary source tissues emitting radiation is described by Equations 2-2 and 2-3 (19):

$$D(r_T) = \sum_{r_s} \left[ \int_0^{\infty} A(r_s, t) dt \right] S(r_T \leftarrow r_s) = \sum_{r_s} \tilde{A}(r_s) S(r_T \leftarrow r_s) \quad (2-2)$$

$$S(r_T \leftarrow r_s) = \sum_i \frac{E_i Y_i \phi(r_T \leftarrow r_s)}{m_T} = \sum_i \Delta_i \Phi(r_T \leftarrow r_s) \quad (2-3)$$

where  $\tilde{A}(r_s)$  is the time-integrated activity or the total number of nuclear transformations occurring in source tissue  $r_s$ ,  $S(r_T \leftarrow r_s)$  is the radionuclide S value, defined as the mean absorbed dose rate to target tissue  $r_T$  per unit activity in source tissue  $r_s$ ,  $E_i$  is the energy of the  $i^{\text{th}}$  radiation,  $Y_i$  is the yield of the  $i^{\text{th}}$  radiation,  $\phi(r_T \leftarrow r_s)$  is the AF, defined as the fraction of radiation energy emitted in source tissue  $r_s$  that is absorbed in target tissue  $r_T$ ,  $m_T$  is the mass of the target tissue  $r_T$ ,  $\Delta_i$  is the delta value for the  $i^{\text{th}}$  radiation, defined as the product of the energy and the yield of the  $i^{\text{th}}$  radiation, and  $\Phi(r_T \leftarrow r_s)$  is the SAF, defined as the ratio of the AF to the target tissue mass.

As discussed previously, the values extracted from the output of the MCNPX simulations were energy deposition per unit mass averaged over the target tissue for the F6 tally and total energy deposition over the target tissue for the \*F8 tally. The unit for the F6 tally was MeV/g, so to obtain the SAF for any particular target tissue, the F6 tally result was divided by the initial photon energy. This method was determined to be accurate because the F6 tally described the amount of energy deposited in the target tissue per unit mass by a single photon emitted in the

source tissue. The deposited energy divided by the emitted energy determined the fraction of that emitted energy that was deposited in the target tissue which is, by definition, the AF. The SAF is defined as the AF divided by the mass of the target tissue, giving units of inverse mass. Due to the small size of the newborn, it was prudent to evaluate the SAFs in units of  $\text{g}^{-1}$ . To determine the SAF from the \*F8 tallies, the \*F8 result was divided by both the initial energy of the photon as well as the calculated mass of the target organ. This was determined to be accurate by the same reasoning as the F6 tally conversion except that the total energy deposited needed to be divided by the total mass of the target tissue to obtain the same original units as the F6 tally.

A different method was used to convert the spongiosa F4 tallies to AM and  $\text{TM}_{50}$  SAFs because the skeletal DRFs were used instead of direct dose or energy tallying. Equation 2-4 was used to calculate the SAFs for both AM and  $\text{AM}_{50}$  target regions for the whole skeleton:

$$\Phi(r_T \leftarrow r_S) = \frac{k}{E_0} \sum_{r_{sp}} w_{r_{sp}} \sum_i \left[ \frac{D(r_T)}{\Psi(E_i)} \right] \Psi(r_{sp} \leftarrow r_S, E_i) \quad (2-4)$$

where  $k$  is a constant that converts to units of  $\text{g}^{-1}$  and was found to be  $6.24142 \times 10^{13} \text{ cm}^2 \cdot \text{MeV} \cdot \text{kg} / \text{m}^2 \cdot \text{J} \cdot \text{g}$ ,  $E_0$  is the initial photon energy,  $w_{r_{sp}}$  is the mass fraction of the target tissue  $r_T$  in each bone site,  $[D(r_T)/\Psi(E_i)]$  is the skeletal DRF for target tissue  $r_T$  (either whole body AM or  $\text{AM}_{50}$ ) at photon energy  $E_i$ ,  $\Psi(r_{sp} \leftarrow r_S, E_i)$  is the photon fluence emitted from source tissue  $r_S$  incident on the spongiosa of the bone site of interest for photons of energy  $E_i$ , and  $\Phi(r_T \leftarrow r_S)$  is the SAF for target tissue  $r_T$  from any source tissue  $r_S$ . The computational MATLAB code, *drfread.m*, developed for Equation 2-4 can be seen in Appendix B.

SAFs were obtained for every source-target-energy combination for both the male and female UF newborn hybrid phantoms. This was deemed a complete set of photon SAFs and thus a complete internal photon dosimetry characterization of the UF newborn hybrid phantoms.

These SAFs can be used to perform dosimetry calculations for *any* nuclear medicine procedure, provided the radiopharmaceutical biokinetics are known.

### **Renal Function Case Study**

Once the dosimetry characterization was completed for the phantoms, it was desired that an application of the new dosimetry be explored. A nuclear medicine imaging procedure typically performed on newborns is one that attempts to assess the renal function, or in the case of newborns, renal function immaturity: technetium-99m-dimercaptosuccinic acid ( $^{99m}\text{Tc}$ -DMSA) SPECT (20). This study attempted to provide a dose estimate for a newborn patient for typical parameters used in the performance of this renal function SPECT procedure.

### **Clinical Aspects**

Two general groups of radiopharmaceuticals used in nuclear medicine imaging of the kidneys are those that quickly clear the kidneys and those that accumulate in the renal parenchyma for a relatively long time (20). Quickly clearing radiopharmaceuticals are used for the assessment of renal function and urine drainage, while slowly clearing radiopharmaceuticals are used for mapping of regional functioning renal parenchyma (20). Static renal scintigraphy performed using SPECT is the preferred method for renal function because of the ability to explore the kidney images in three dimensions. This is preferred over conventional planar scintigraphy because the planar method is not able to map regional functioning renal parenchyma.

The procedure is performed using the radiopharmaceutical  $^{99m}\text{Tc}$ -DMSA. The patient is injected with the radiopharmaceutical and instructed to wait approximately 4 hours in order to allow the radionuclide to decay. The patient is then scanned using a three-detector array of gamma cameras. Scan times range from about 15 to 20 minutes to acquire approximately 120 images on a 128 x 128 pixel matrix (20).

## Dosimetry Assessment

### Biokinetics

The first analysis performed in order to accurately determine a whole-body effective dose was the characterization of  $^{99m}\text{Tc}$ -DMSA biokinetics. Residence times,  $t_{res}$ , which take into account both radioactive and biological half-lives were calculated for each organ that retains the radiopharmaceutical, considered source organs, as described by  $\tilde{A}(r_s)$  in Equation 2-2.  $\tilde{A}(r_s)$  is in units of total number of nuclear transformations in source tissue  $r_s$ . This was defined as the administered activity multiplied by  $t_{res}$  for each source organ. The source organs were determined to be the left and right kidneys (the kidney cortex was assumed to receive all of the kidney activity), liver, spleen, urinary bladder contents, heart contents, lungs, and rest of body (21,22,23). The biodistribution parameters for the newborn can be seen in Table 2-4 (21,23). Blood kinetics were analyzed separately to obtain lung and heart contents residence times.

From the information in Table 2-4 as well as additional information not reported here, residence times were calculated based on Equations 2-2 and 2-5 (24):

$$A(t) = A_m \left(1 - e^{-\lambda_+ t}\right) e^{-(\lambda_- + \lambda_p) t} \quad (2-5)$$

where  $A_m$  is fractional maximum uptake,  $A_o$  is fractional initial uptake,  $\lambda_+$  is the uptake rate in  $\text{h}^{-1}$ ,  $\lambda_-$  is the clearance rate in  $\text{h}^{-1}$ ,  $\lambda_{eff}$  is the effective clearance rate in  $\text{h}^{-1}$ , and  $A(t)$  is the time dependent fractional injected activity. Equation 2-5 was integrated from zero to infinity to obtain the organ specific radiopharmaceutical residence times, as indicated in Equation 2-2. Detailed biokinetic analysis was beyond the scope of this study, so the biokinetic calculations were simply patterned after a previous execution of this analysis (22).

## Whole-body effective dose

Once the source organ residence times were obtained, individual equivalent organ doses were determined as well as a whole-body effective dose. Dose calculations were normalized to the injected activity to facilitate the comparison between dose calculations based on the UF newborn hybrid phantom and a previous study using stylized phantom. The formalism for calculating organ and whole body absorbed dose has already been described by Equations 2-3 and 2-4. Individual organ equivalent doses were determined by Equation 2-6, and the whole body effective dose was calculated using Equation 2-7 (25):

$$H_{r_T} = \sum_R w_R D_{r_T,R} \quad (2-6)$$

$$E = \sum_{r_T} w_{r_T} H_{r_T} \quad (2-7)$$

where  $w_R$  is the radiation weighting factor for radiation type  $R$ ,  $w_{r_T}$  is the organ weighting factor for target organ  $r_T$ ,  $D_{r_T,R}$  is the absorbed dose to target organ  $r_T$  from radiation type  $R$  in units of mGy / MBq,  $H_{r_T}$  is the organ specific equivalent dose in units of mSv / MBq, and  $E$  is the whole body effective dose in units of mSv / MBq.

The radiation weighting factor is based on the linear energy transfer (LET) characteristics of the incident radiation type. For photons, the radiation weighting factor is one, so the organ specific equivalent dose is equal to the absorbed dose. The organ weighting factors are based on radiation stochastic risk data and takes into account lifetime cancer incidence, dose and dose-rate effectiveness, lethality, quality of life for non-fatal cancers, and years of life lost (25). The study used for comparison utilized the tissue weighting factors recommended by ICRP 30, so for consistency these values were used despite the fact that more recent tissue weighting factors have been developed (20).

Tc-99m has a radioactive half-life of 6.02 hours and decays primarily by isomeric transition with a principal gamma-ray energy of 140.5 keV and yield of 0.8906 at this energy (26). The SAF was obtained by interpolation between 0.1 and 0.15 MeV. By applying the gamma-ray energy, radiation yield, source organ residence times, radiation weighting factor, target organ weighting factors, and energy- and organ-dependent SAFs, the individual organ equivalent doses and whole-body effective dose were obtained.

The application of the methods described for the dosimetry of the renal function case study yields the photon component of the whole-body effective dose. To compare the results to a previous determination of organ equivalent doses and whole-body effective dose, an estimate of the electron component of the absorbed dose must be made. As a rough estimate, the absorbed fractions for electrons were set to one when the source and target tissues were the same and zero when the source and target tissues were different. Delta values were used to convert the SAFs calculate for the electrons to radionuclide S values, which were then converted to normalized dose by multiplying by the residence times in each source organ. The delta values, in units of Gy · kg / nuclear transformation, were obtained from the latest MIRDOSE series of radioactive decay data for  $\beta^-$ , internal conversion, and Auger electrons. Obviously, an estimate of electron dose does not generate the most accurate estimate of organ equivalent or whole-body effective dose, but the purpose of the renal function case study was to demonstrate the ease of application to a real world situation rather than provide exact dose calculations for renal function SPECT imaging.

Table 2-1. Active marrow distribution in the UF newborn hybrid phantom compared to active marrow distribution for the reference newborn in ICRP 89 (14).

<b>Skeletal Site</b>	<b>NURBS / Polygon Mesh (%)</b>	<b>ICRP 89 Table 9.4 (%)</b>	<b>Difference (%)</b>	<b>Ratio NURBS / ICRP</b>
Cranium	24.12	27.00	-2.88	0.89
Mandible	4.33	2.50	1.83	1.73
Cervical Vertebrae	3.73	3.40	0.33	1.10
Thoracic Vertebrae	5.16	8.30	-3.14	0.62
Lumbar Vertebrae	4.70	2.40	2.30	1.96
Sternum	0.51	0.00	0.51	
Ribs	16.28	9.20	7.08	1.77
Scapulae	3.23	2.70	0.53	1.20
Clavicles	1.22	0.80	0.42	1.52
Os coxae	6.31	9.20	-2.89	0.69
Sacrum	1.88	0.10	1.78	18.83
Humeri, Proximal	2.12			
Humeri, Upper Shaft	0.45	2.30	0.27	1.12
Humeri, Lower Shaft	0.45			
Humeri, Distal	1.66	2.30	-0.19	0.92
Radii, Proximal	0.36			
Radii, Shaft	0.17	1.10	0.08	1.08
Radii, Distal	0.65			
Ulnae, Proximal	0.86			
Ulnae, Shaft	0.20	1.40	0.09	1.07
Ulnae, Distal	0.44			
Wrists and Hands	2.42	3.60	-1.18	0.67
Femora, Proximal	3.46			
Femora, Upper Shaft	1.03	3.70	0.79	1.21
Femora, Lower Shaft	1.64			
Femora, Distal	2.86	3.70	0.80	1.22
Patellae	0.13	0.13	0.01	1.07
Tibiae, Proximal	2.46			
Tibiae, Shaft	0.94	6.43	-1.53	0.76
Tibiae, Distal	1.51			
Fibulae, Proximal	0.33			
Fibulae, Shaft	0.15	1.44	-0.46	0.68
Fibulae, Distal	0.50			
Ankles and Feet	3.75	8.30	-4.55	0.45
<b>Total</b>	<b>100.00</b>	<b>100.00</b>	<b>0.00</b>	

Table 2-2. Mineral bone (trabecular and cortical bone) distribution in the UF newborn hybrid phantoms (14).

Skeletal Site	Volumes and Masses Including MST			
	Trabecular Bone* (cm <sup>3</sup> )	Trabecular Bone* (g)	Cortical Bone* (cm <sup>3</sup> )	Cortical Bone* (g)
Cranium	35.44	56.06	12.90	20.41
Mandible	1.49	2.36	1.02	1.62
Cervical Vertebrae	2.57	4.07	2.27	3.58
Thoracic Vertebrae	3.92	6.20	5.14	8.13
Lumbar Vertebrae	2.59	4.09	1.64	2.59
Sternum	0.18	0.28	0.10	0.17
Ribs	5.60	8.86	3.84	6.08
Scapulae	1.23	1.95	1.47	2.32
Clavicles	0.46	0.73	0.55	0.87
Os coxae	2.40	3.80	3.70	5.85
Sacrum	1.04	1.64	0.66	1.04
Humeri, Proximal	1.16	1.84	0.23	0.36
Humeri, Upper Shaft	0.00	0.00	0.94	1.48
Humeri, Lower Shaft	0.00	0.00	0.93	1.47
Humeri, Distal	0.91	1.45	0.18	0.29
Radii, Proximal	0.20	0.31	0.04	0.06
Radii, Shaft	0.00	0.00	0.63	0.99
Radii, Distal	0.35	0.56	0.07	0.11
Ulnae, Proximal	0.47	0.75	0.09	0.15
Ulnae, Shaft	0.00	0.00	0.80	1.27
Ulnae, Distal	0.24	0.38	0.05	0.08
Wrists and Hands	0.83	1.32	0.50	0.79
Femora, Proximal	1.90	3.01	0.37	0.59
Femora, Upper Shaft	0.00	0.00	1.89	2.98
Femora, Lower Shaft	0.00	0.00	3.00	4.74
Femora, Distal	1.57	2.49	0.31	0.49
Patellae	0.05	0.07	0.03	0.04
Tibiae, Proximal	1.35	2.14	0.27	0.42
Tibiae, Shaft	0.00	0.00	2.27	3.58
Tibiae, Distal	0.83	1.31	0.16	0.26
Fibulae, Proximal	0.18	0.28	0.04	0.06
Fibulae, Shaft	0.00	0.00	0.61	0.96
Fibulae, Distal	0.28	0.44	0.05	0.09
Ankles and Feet	1.29	2.04	0.78	1.23
<b>Total Skeleton</b>	<b>68.54</b>	<b>108.43</b>	<b>47.52</b>	<b>75.17</b>
<b>ICRP 89 Reference</b>	<b>N/A</b>	<b>N/A</b>	<b>N/A</b>	<b>N/A</b>
<b>Ratio</b>	<b>N/A</b>	<b>N/A</b>	<b>N/A</b>	<b>N/A</b>

\*Denotes inclusion of associated miscellaneous skeletal tissue volumes and masses

Table 2-3. A list of all the source organs for the male and female UF newborn hybrid phantoms.

Residual soft tissue	Larynx	Spleen
Adrenal (L)	Lens	Stomach wall
Adrenal (R)	Liver	Stomach contents
Brain	Lung (L)	Testes
Breast	Lung (R)	Thymus
Bronchi	Nasal layer (anterior)	Thyroid
Right colon wall	Nasal layer (posterior)	Tongue
Right colon contents	Oral cavity layer	Tonsil
Ears	Ovaries	Trachea
Esophagus	Pancreas	Urinary bladder wall
External nose	Penis	Urinary bladder contents
Eye balls	Pharynx	Uterus
Gall bladder wall	Prostate	Air (in body)
Gall bladder contents	Pituitary gland	Left colon wall
Heart wall	Rectosigmoid wall	Left colon contents
Heart contents	Rectosigmoid contents	Salivary glands (submaxillary)
Kidney-cortex (L)	Salivary glands (parotid)	Salivary glands (sublingual)
Kidney-cortex (R)	Scrotum	Cartilage
Kidney-medulla (L)	Small intestine wall	Active marrow
Kidney-medulla (R)	Small intestine contents	Trabecular bone
Kidney-pelvis (L)	Skin	Cortical bone
Kidney-pelvis (R)	Spinal cord	

Table 2-4. Biokinetic parameters for  $^{99m}\text{Tc}$ -DMSA for the newborn patient (22)\*.

	$A_m$	$A_o$	$\lambda_+$ ( $\text{h}^{-1}$ )	$\lambda_-$ ( $\text{h}^{-1}$ )	$\lambda_{\text{eff.}}$ ( $\text{h}^{-1}$ )	Fraction Excreted	
						6 h	24 h
Left kidney	0.21	--	0.72	0.009	--	--	--
Right kidney	0.21	--	0.64	0.008	--	--	--
Liver	--	0.057	--	--	0.14	--	--
Spleen	--	0.016	--	--	0.16	--	--
Urinary bladder contents	--	--	--	--	--	0.066	0.13
Whole body	--	--	--	--	--	--	--

\*  $A_m$  is fractional maximum uptake,  $A_o$  is fractional initial uptake,  $\lambda_+$  is the uptake rate,  $\lambda_-$  is the clearance rate, and  $\lambda_{\text{eff.}}$  is the effective clearance rate.

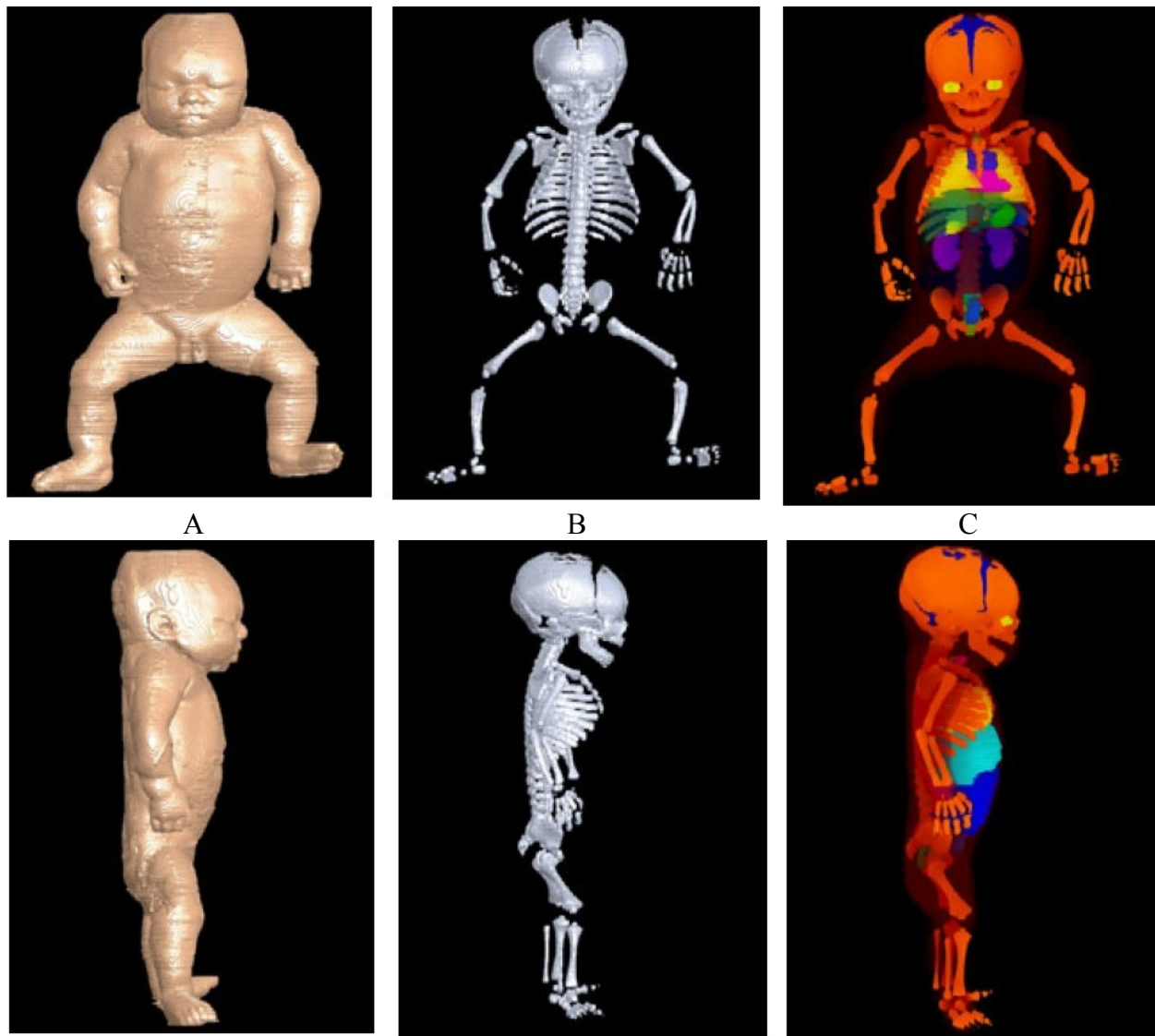


Figure 2-1. Coronal and sagittal views of the UF newborn voxel computational dosimetry phantom (13). A) Outer body contour. B) Skeleton. C) Principal internal organs.

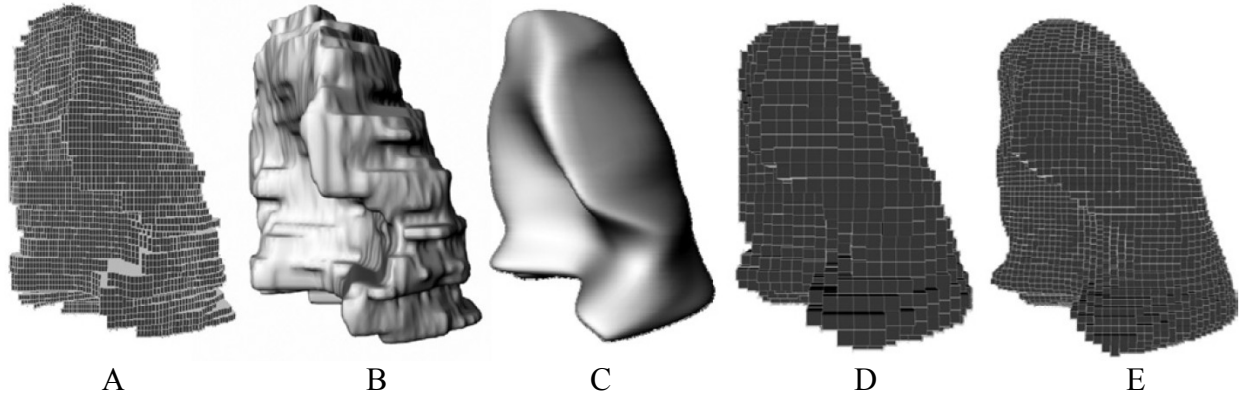


Figure 2-2. Steps in the process of converting the original newborn voxel model into a NURBS model and voxelizing for input into MCNPX (12). A) Original voxel geometry. B) Polygon mesh geometry. C) NURBS geometry. D) Voxelization of NURBS volume at  $(2\text{ mm})^3$  resolution. E) Voxelization of NURBS volume at  $(1\text{ mm})^3$  resolution.

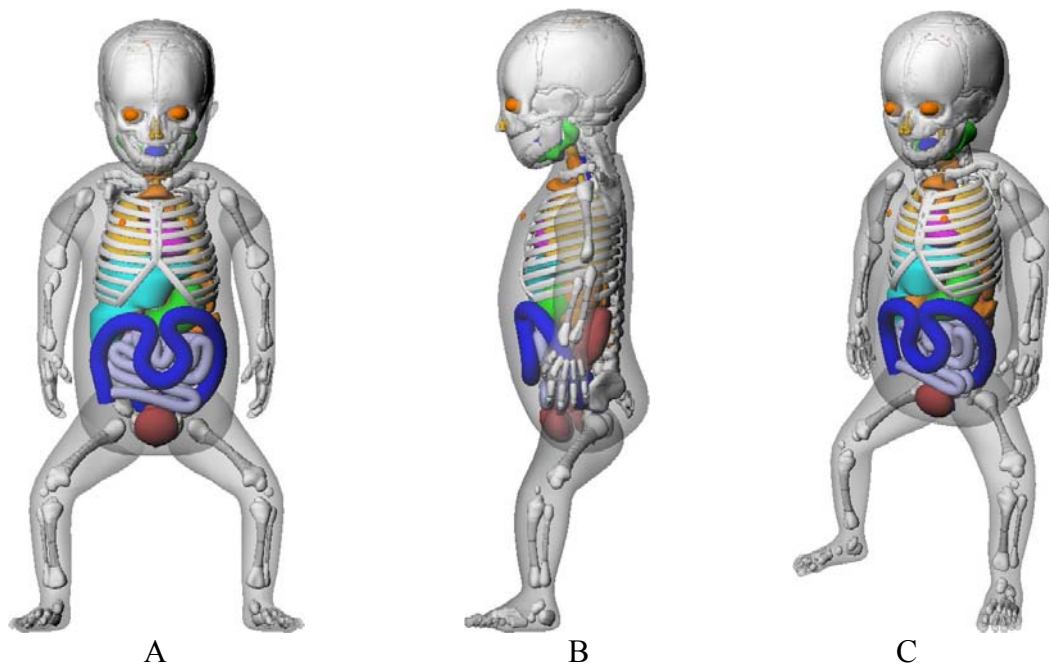


Figure 2-3. The UF newborn hybrid female phantom. A) Coronal view. B) Sagittal view. C) Perspective view.

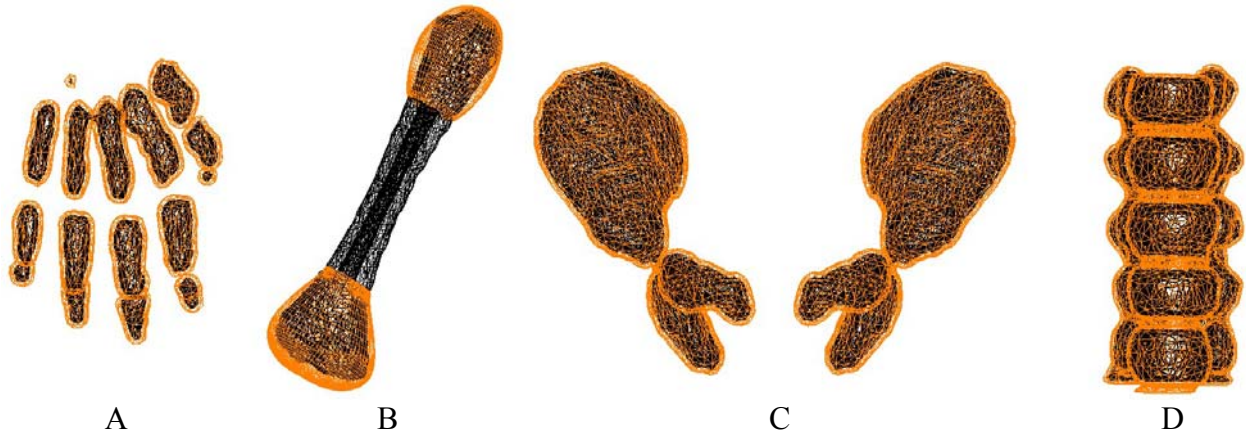


Figure 2-4. Sample bone sites of the UF newborn hybrid phantom heterogeneous skeleton. A) Hand. B) Right Humerus. C) Pelvis. D) L-spine.

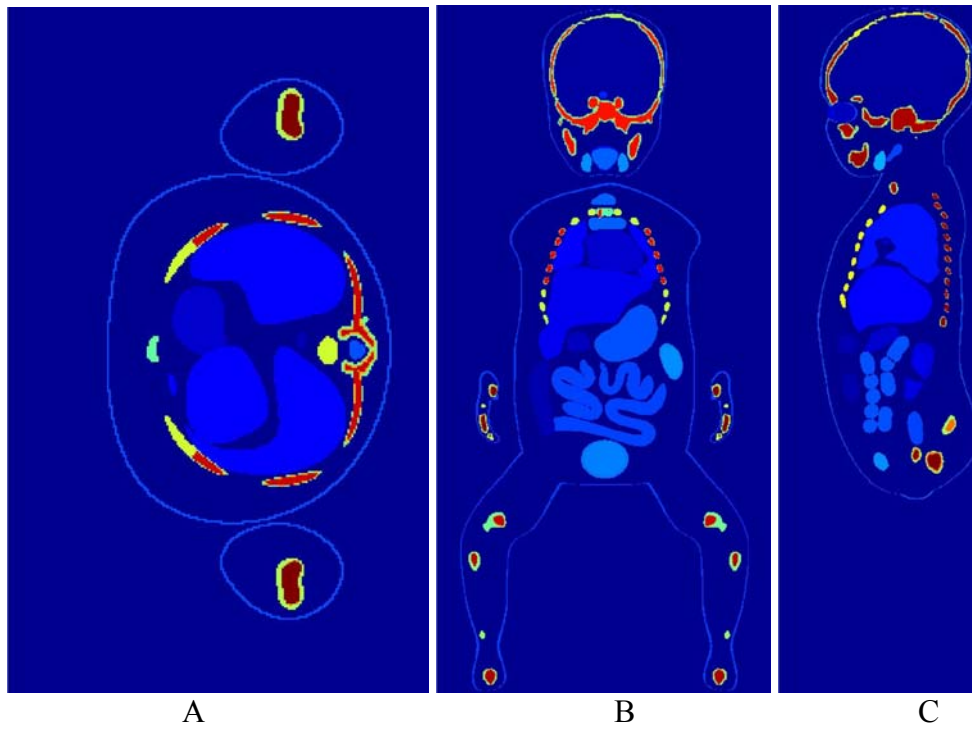


Figure 2-5. UF newborn hybrid female phantom voxelized at a resolution of  $(0.663 \text{ mm})^3$ . A) Axial view. B) Coronal view. C) Sagittal view.

## CHAPTER 3 RESULTS

### **Skeletal Dose Response Functions**

A representative bone site to display the results from the DRF analysis was chosen to be the mandible, and the DRFs and kerma response functions for the mandible can be seen in Figure 3-1. The results were shown with units of absorbed dose per unit photon fluence or  $\text{Gy} \cdot \text{m}^2 / \text{photon}$ . As shown in Equation 2-4, a unit conversion factor was needed to convert the original DRF units to the final desired SAF units of  $\text{g}^{-1}$ .

Examining first the DRF calculated for the AM target, it should be noted that the source was total spongiosa which was comprised of both AM and TB. The dose response was assessed for a fluence of photons incident on the spongiosa. In turn, the electrons liberated in both AM and TB were considered the source. Also note that the total AM region *includes* the  $\text{TM}_{50}$ , but not vice versa. The AM DRF originates at a value just below  $10^{-15} \text{Gy} \cdot \text{m}^2 / \text{photon}$  for a low photon energy of 0.01 MeV. This was due to the fact that the resultant secondary electrons, initiated at a comparable low energy, possessed very short ranges and thus primarily deposited most of their energy at the site in which they were born. As the incident photon energy increases to about 90 keV, the DRF declines because the electrons begin to attain energies capable of transporting them into nearby trabeculae, thus delivering less dose to the AM. As the incident photon energy increases past 90 keV, the DRF increases because the secondary electrons have enough energy to penetrate completely through the trabeculae and into adjacent regions of AM. At high energies greater than 1 MeV, the DRF begins to decline because the DRF calculations were based on AF data which assumed that all initiated electrons attain enough energy to mostly escape from the spongiosa into the cortical bone (16). However, as will be discussed later, this model was not the most accurate.

The shape of the  $TM_{50}$  (bone endosteum) DRF can be explained in the same way as the AM DRF. However, it is evident that at intermediate incident photon energies, the  $TM_{50}$  DRF is slightly greater than the AM DRF. This is because as incident photon energy increases the secondary electrons that escape the TB regions terminate in the  $AM_{50}$  before they attain enough energy to penetrate through the  $TM_{50}$  region into the AM region.

While the above discussion of the results of the DRF analysis describes some of the physics taking place, the shapes of the curves cannot be described completely in this manner. The DRFs are heavily dependent on the shape of the energy- and atomic composition-dependent photon interaction cross sections. This is evidenced by Equation 2-1.

As previously noted, the DRFs were calculated based on AF data which assumed secondary electron escape from the spongiosa into the surrounding cortical bone. However, this model did not take into account secondary electrons born in the surrounding cortical bone entering the spongiosa. At high enough incident photon energies, this is the case, and it creates a sort of charged particle equilibrium (CPE). In this CPE scenario, electrons escaping a particular microstructure are replaced by electrons entering the microstructure from the cortical bone. Physically, this process can be represented by ignoring the DRF considering escape and thinking of the secondary electrons as depositing all of their initiated energy at the site of interaction. Kerma describes this physical process exactly. Therefore, it was decided that the calculated DRFs would be accepted up until the point at which the DRFs began to deviate from the kerma response functions. At this deviation point, the DRFs were cut off and replaced by the results from the kerma response functions, forming a sort of hybrid DRF. It can be seen that there is a slight difference between the kerma response for spongiosa and the kerma response for AM. The kerma response for spongiosa was chosen to complete the skeletal DRFs because there is no

microstructure present in the dosimetry phantoms. The spongiosa region was the only region that was able to be tallied for photon fluence. The complete hybrid DRF results can be seen in Figure 3-2.

### **Specific Absorbed Fractions**

A representative source tissue was selected to display the results of the SAF calculations, and this source tissue was chosen to be the liver of the UF newborn female hybrid phantom. The SAFs for the liver source can be seen in Table 3-1. A plot of the SAFs for selected target organs can be seen in Figure 3-3. The average error over all target organs and energies was ~1%, which was considered acceptable. Similar errors were seen across all source-target-energy combinations.

The purpose of this section is to simply present the results. The results will be compared to SAFs obtained for the newborn stylized phantom by ORNL in the next section. It will be seen that there were notable differences between the SAFs found from the UF newborn hybrid phantom and the ORNL newborn stylized phantom.

### **Renal Function Case Study**

The residence times calculated from the newborn patient biokinetic data for  $^{99m}\text{Tc}$ -DMSA can be seen in Table 3-2. These residence times were used to calculate the photon and electron components of the organ equivalent doses and those results can be seen in Table 3-3 along with the associated tissue weighting factors for each target organ. Using Table 3-3, a whole-body effective dose of  $1.63 \times 10^{-1}$  mSv / MBq was calculated for the UF newborn female hybrid phantom using the ICRP 30 tissue weighting factors and  $7.52 \times 10^{-2}$  mSv / MBq using the ICRP 103 tissue weighting factors. Tc-99m-DMSA is usually given with a dose of 1.5 to 1.9 MBq / kg (20). For the UF newborn female hybrid phantom, whose total mass was ~3.5 kg, a typical whole-body effective dose was found to be between 0.84 and 1.06 mSv for the ICRP 30 tissue

weighting factors and 0.39 and 0.49 mSv for the ICRP 103 tissue weighting factors. For comparison, a year's dose of natural background radiation is about 1 mSv.

Table 3-1. Specific absorbed fractions in units of g-1 for the liver source in the female UF newborn hybrid phantom.

Target	Energy (MeV)								
	0.01	0.015	0.02	0.03	0.04	0.05	0.06	0.08	0.1
Residual Soft Tissue	2.76E-05	7.00E-05	1.11E-04	1.25E-04	9.84E-05	7.59E-05	6.22E-05	4.98E-05	4.58E-05
Adrenal (L)	1.66E-08	1.72E-05	1.22E-04	2.54E-04	2.22E-04	1.76E-04	1.44E-04	1.14E-04	1.03E-04
Adrenal (R)	1.01E-04	5.60E-04	9.55E-04	8.55E-04	5.72E-04	4.06E-04	3.19E-04	2.47E-04	2.25E-04
Brain	0.00E+00	1.89E-11	5.52E-09	6.68E-07	2.15E-06	2.88E-06	3.10E-06	3.12E-06	3.13E-06
Breast	0.00E+00	2.80E-06	3.45E-05	9.94E-05	9.23E-05	7.35E-05	6.18E-05	5.07E-05	4.71E-05
Bronchi	0.00E+00	9.85E-06	9.14E-05	1.95E-04	1.68E-04	1.32E-04	1.08E-04	8.50E-05	7.67E-05
Right Colon W	5.53E-05	1.90E-04	3.23E-04	3.47E-04	2.56E-04	1.89E-04	1.51E-04	1.18E-04	1.07E-04
Right Colon C	1.62E-05	1.39E-04	2.88E-04	3.34E-04	2.50E-04	1.85E-04	1.48E-04	1.16E-04	1.05E-04
Ears	0.00E+00	0.00E+00	1.98E-07	3.50E-06	5.84E-06	6.13E-06	5.95E-06	5.53E-06	5.45E-06
Esophagus	1.53E-05	1.51E-04	3.17E-04	3.49E-04	2.56E-04	1.90E-04	1.53E-04	1.19E-04	1.08E-04
External nose	0.00E+00	1.51E-07	3.41E-06	1.45E-05	1.54E-05	1.34E-05	1.20E-05	1.04E-05	1.00E-05
Eye balls	0.00E+00	0.00E+00	1.22E-07	2.59E-06	5.41E-06	6.21E-06	6.23E-06	5.96E-06	5.88E-06
Gall Bladder W	2.18E-04	1.04E-03	1.58E-03	1.26E-03	8.08E-04	5.61E-04	4.36E-04	3.36E-04	3.06E-04
Gall Bladder C	1.00E-04	8.75E-04	1.50E-03	1.25E-03	8.04E-04	5.59E-04	4.34E-04	3.40E-04	3.05E-04
Heart W	6.44E-05	2.88E-04	5.14E-04	5.09E-04	3.58E-04	2.59E-04	2.05E-04	1.59E-04	1.45E-04
Heart C	6.59E-06	1.60E-04	4.22E-04	4.86E-04	3.52E-04	2.57E-04	2.04E-04	1.58E-04	1.43E-04
Kidney-cortex (L)	0.00E+00	8.54E-07	2.21E-05	9.65E-05	1.03E-04	8.87E-05	7.54E-05	6.07E-05	5.49E-05
Kidney-cortex (R)	6.45E-05	3.88E-04	6.53E-04	5.92E-04	4.05E-04	2.91E-04	2.30E-04	1.78E-04	1.63E-04
Kidney-medulla (L)	0.00E+00	6.91E-07	2.27E-05	1.03E-04	1.10E-04	9.42E-05	8.00E-05	6.42E-05	5.78E-05
Kidney-medulla (R)	5.09E-06	2.03E-04	4.95E-04	5.29E-04	3.77E-04	2.74E-04	2.17E-04	1.68E-04	1.53E-04
Kidney-pelvis (L)	0.00E+00	4.03E-07	1.98E-05	9.83E-05	1.07E-04	9.19E-05	7.85E-05	6.30E-05	5.69E-05
Kidney-pelvis (R)	5.75E-07	1.18E-04	3.80E-04	4.62E-04	3.41E-04	2.51E-04	2.00E-04	1.55E-04	1.40E-04
Larynx	0.00E+00	3.41E-08	2.42E-06	2.37E-05	3.19E-05	3.02E-05	2.70E-05	2.28E-05	2.10E-05
Lens	0.00E+00	0.00E+00	3.75E-07	3.48E-06	5.80E-06	6.36E-06	6.15E-06	5.79E-06	5.73E-06
Liver	7.33E-03	6.19E-03	4.67E-03	2.36E-03	1.32E-03	8.75E-04	6.72E-04	5.25E-04	4.90E-04
Lung (L)	1.66E-05	9.06E-05	1.92E-04	2.46E-04	1.94E-04	1.47E-04	1.17E-04	8.98E-05	8.00E-05
Lung (R)	5.14E-05	2.96E-04	5.32E-04	5.20E-04	3.61E-04	2.58E-04	2.01E-04	1.52E-04	1.36E-04
Nasal layer (anterior)	0.00E+00	1.32E-07	3.80E-06	1.56E-05	1.63E-05	1.40E-05	1.26E-05	1.08E-05	1.03E-05
Nasal layer (posterior)	0.00E+00	6.15E-09	1.93E-07	3.66E-06	7.04E-06	7.81E-06	7.72E-06	7.28E-06	7.09E-06
Oral cavity layer	0.00E+00	4.52E-09	1.10E-06	1.49E-05	2.17E-05	2.12E-05	1.92E-05	1.66E-05	1.55E-05
Ovaries	0.00E+00	1.99E-07	7.02E-06	4.43E-05	5.42E-05	4.94E-05	4.28E-05	3.54E-05	3.19E-05
Pancreas	0.00E+00	8.56E-06	7.99E-05	1.93E-04	1.74E-04	1.39E-04	1.15E-04	9.00E-05	8.08E-05
Pharynx	0.00E+00	0.00E+00	4.64E-07	9.47E-06	1.57E-05	1.62E-05	1.51E-05	1.34E-05	1.25E-05
Pituitary Gland	0.00E+00	0.00E+00	0.00E+00	8.40E-07	3.28E-06	4.58E-06	4.96E-06	5.09E-06	4.96E-06
Rectosigmoid W	0.00E+00	3.19E-07	6.55E-06	3.63E-05	4.48E-05	4.14E-05	3.65E-05	3.04E-05	2.77E-05
Rectosigmoid C	0.00E+00	2.82E-07	6.34E-06	3.73E-05	4.63E-05	4.27E-05	3.76E-05	3.13E-05	2.85E-05
Salivary Glands (parotid)	0.00E+00	5.69E-09	4.83E-07	9.21E-06	1.49E-05	1.52E-05	1.42E-05	1.25E-05	1.18E-05
SI W	2.01E-05	7.04E-05	1.41E-04	1.94E-04	1.61E-04	1.26E-04	1.03E-04	8.11E-05	7.32E-05
SI C	6.69E-06	5.48E-05	1.31E-04	1.91E-04	1.60E-04	1.25E-04	1.02E-04	8.07E-05	7.28E-05
Skin	6.93E-08	6.79E-06	2.84E-05	5.15E-05	4.53E-05	3.66E-05	3.07E-05	2.54E-05	2.38E-05
Spinal Cord	0.00E+00	3.11E-06	3.46E-05	1.16E-04	1.19E-04	1.01E-04	8.64E-05	7.09E-05	6.54E-05
Spleen	1.42E-08	1.33E-05	9.01E-05	1.92E-04	1.69E-04	1.34E-04	1.10E-04	8.72E-05	7.87E-05
Stomach W	7.86E-05	2.98E-04	5.15E-04	5.30E-04	3.81E-04	2.79E-04	2.21E-04	1.71E-04	1.55E-04
Stomach C	1.43E-05	1.71E-04	4.09E-04	4.83E-04	3.58E-04	2.64E-04	2.11E-04	1.63E-04	1.47E-04
Thymus	0.00E+00	2.08E-06	3.43E-05	1.09E-04	1.05E-04	8.66E-05	7.24E-05	5.77E-05	5.23E-05
Thyroid	0.00E+00	2.50E-08	3.51E-06	2.95E-05	3.80E-05	3.51E-05	3.12E-05	2.61E-05	2.39E-05
Tongue	0.00E+00	6.15E-09	1.32E-06	1.68E-05	2.39E-05	2.31E-05	2.08E-05	1.79E-05	1.66E-05
Tonsil	0.00E+00	0.00E+00	7.28E-07	1.23E-05	1.97E-05	1.94E-05	1.80E-05	1.54E-05	1.44E-05
Trachea	0.00E+00	9.63E-07	1.98E-05	7.56E-05	7.80E-05	6.63E-05	5.64E-05	4.56E-05	4.12E-05
Urinary bladder W	0.00E+00	1.42E-08	1.33E-06	1.64E-05	2.40E-05	2.34E-05	2.13E-05	1.81E-05	1.68E-05
Urinary bladder C	0.00E+00	6.52E-09	1.17E-06	1.55E-05	2.31E-05	2.26E-05	2.07E-05	1.77E-05	1.63E-05
Uterus	0.00E+00	2.10E-08	2.23E-06	2.36E-05	3.29E-05	3.13E-05	2.82E-05	2.38E-05	2.18E-05
Air (in body)	1.78E-04	1.85E-02	8.54E-02	1.68E-01	1.50E-01	1.21E-01	1.00E-01	8.08E-02	7.46E-02
Left Colon W	2.67E-08	6.21E-06	4.01E-05	1.04E-04	1.00E-04	8.26E-05	6.91E-05	5.53E-05	5.00E-05
Left Colon C	1.02E-08	4.97E-06	3.73E-05	1.02E-04	9.93E-05	8.23E-05	6.90E-05	5.50E-05	4.98E-05
Salivary Glands (submaxillary)	0.00E+00	0.00E+00	1.62E-06	1.79E-05	2.50E-05	2.37E-05	2.13E-05	1.82E-05	1.70E-05
Salivary Glands (sublingual)	0.00E+00	1.76E-08	3.26E-06	2.45E-05	3.06E-05	2.79E-05	2.48E-05	2.09E-05	1.93E-05
Cartilage	1.07E-09	7.53E-09	1.78E-08	3.05E-08	3.16E-08	2.97E-08	2.83E-08	2.83E-08	3.10E-08
Active Marrow (AM)	1.63E-06	1.30E-05	3.54E-05	6.42E-05	6.33E-05	5.69E-05	5.09E-05	4.63E-05	3.98E-05
Endosteum (AM50)	1.58E-06	1.28E-05	3.55E-05	6.75E-05	6.91E-05	6.28E-05	5.60E-05	4.60E-05	4.04E-05

Table 3-1. Continued.

Energy (MeV)												
0.15	0.2	0.3	0.4	0.5	0.6	0.8	1	1.5	2	3	4	
4.47E-05	4.56E-05	4.70E-05	4.75E-05	4.75E-05	4.71E-05	4.60E-05	4.47E-05	4.13E-05	3.84E-05	3.39E-05	3.07E-05	
9.88E-05	1.00E-04	1.00E-04	1.00E-04	9.85E-05	9.75E-05	9.51E-05	9.29E-05	8.44E-05	7.80E-05	6.82E-05	6.22E-05	
2.17E-04	2.20E-04	2.23E-04	2.24E-04	2.24E-04	2.22E-04	2.15E-04	2.07E-04	1.91E-04	1.80E-04	1.58E-04	1.41E-04	
3.33E-06	3.61E-06	4.05E-06	4.38E-06	4.58E-06	4.72E-06	4.88E-06	4.96E-06	4.93E-06	4.85E-06	4.57E-06	4.31E-06	
4.33E-05	5.03E-05	4.68E-05	4.92E-05	5.19E-05	5.09E-05	4.55E-05	4.77E-05	4.42E-05	3.79E-05	3.59E-05	3.00E-05	
7.21E-05	6.96E-05	7.06E-05	6.94E-05	6.85E-05	7.02E-05	6.80E-05	6.71E-05	5.84E-05	5.39E-05	4.82E-05	4.34E-05	
1.05E-04	1.06E-04	1.09E-04	1.10E-04	1.09E-04	1.08E-04	1.04E-04	1.00E-04	9.26E-05	8.54E-05	7.57E-05	6.80E-05	
1.01E-04	1.03E-04	1.05E-04	1.05E-04	1.04E-04	1.03E-04	1.00E-04	9.68E-05	8.94E-05	8.23E-05	7.36E-05	6.73E-05	
6.00E-06	5.97E-06	6.64E-06	6.73E-06	7.22E-06	7.79E-06	7.49E-06	6.96E-06	7.13E-06	6.98E-06	5.29E-06	5.33E-06	
1.04E-04	1.07E-04	1.07E-04	1.07E-04	1.07E-04	1.05E-04	1.03E-04	9.89E-05	9.08E-05	8.23E-05	7.28E-05	6.73E-05	
9.84E-06	1.11E-05	1.22E-05	1.28E-05	1.19E-05	1.13E-05	1.21E-05	1.00E-05	1.16E-05	1.01E-05	7.92E-06	7.29E-06	
5.95E-06	6.51E-06	7.22E-06	7.65E-06	7.72E-06	8.02E-06	7.81E-06	7.84E-06	7.42E-06	7.67E-06	6.77E-06	6.14E-06	
3.01E-04	3.03E-04	3.11E-04	3.10E-04	3.07E-04	3.03E-04	2.92E-04	2.82E-04	2.60E-04	2.40E-04	2.10E-04	1.85E-04	
2.97E-04	3.03E-04	3.10E-04	3.11E-04	3.09E-04	3.05E-04	2.95E-04	2.86E-04	2.60E-04	2.42E-04	2.12E-04	1.89E-04	
1.40E-04	1.43E-04	1.46E-04	1.46E-04	1.45E-04	1.43E-04	1.39E-04	1.33E-04	1.23E-04	1.14E-04	1.00E-04	9.03E-05	
1.37E-04	1.38E-04	1.40E-04	1.40E-04	1.38E-04	1.38E-04	1.34E-04	1.28E-04	1.19E-04	1.11E-04	9.83E-05	8.95E-05	
5.05E-05	5.07E-05	5.12E-05	5.11E-05	5.09E-05	4.99E-05	4.86E-05	4.74E-05	4.44E-05	4.15E-05	3.68E-05	3.45E-05	
1.57E-04	1.60E-04	1.63E-04	1.63E-04	1.62E-04	1.59E-04	1.55E-04	1.50E-04	1.37E-04	1.27E-04	1.12E-04	9.99E-05	
5.41E-05	5.38E-05	5.44E-05	5.45E-05	5.35E-05	5.26E-05	5.12E-05	5.01E-05	4.64E-05	4.28E-05	3.85E-05	3.45E-05	
1.45E-04	1.47E-04	1.50E-04	1.51E-04	1.51E-04	1.48E-04	1.44E-04	1.39E-04	1.28E-04	1.17E-04	1.03E-04	9.46E-05	
5.50E-05	5.39E-05	5.46E-05	5.38E-05	5.35E-05	5.36E-05	5.38E-05	5.14E-05	4.73E-05	4.39E-05	3.84E-05	3.58E-05	
1.32E-04	1.34E-04	1.34E-04	1.35E-04	1.33E-04	1.32E-04	1.26E-04	1.21E-04	1.09E-04	1.03E-04	9.22E-05	8.80E-05	
2.00E-05	2.02E-05	1.97E-05	2.10E-05	2.13E-05	2.09E-05	2.06E-05	2.15E-05	1.99E-05	1.78E-05	1.56E-05	1.44E-05	
5.97E-06	8.50E-06	9.27E-06	1.05E-05	9.62E-06	1.04E-05	1.11E-05	1.09E-05	5.63E-06	7.53E-06	8.23E-06	4.93E-06	
4.94E-04	5.12E-04	5.32E-04	5.36E-04	5.33E-04	5.25E-04	5.04E-04	4.81E-04	4.22E-04	3.73E-04	2.99E-04	2.48E-04	
7.42E-05	7.47E-05	7.54E-05	7.52E-05	7.47E-05	7.37E-05	7.17E-05	6.89E-05	6.42E-05	5.91E-05	5.29E-05	4.84E-05	
1.29E-04	1.31E-04	1.33E-04	1.33E-04	1.33E-04	1.31E-04	1.28E-04	1.23E-04	1.13E-04	1.05E-04	9.35E-05	8.40E-05	
8.90E-06	8.87E-06	8.37E-06	1.07E-05	1.23E-05	1.21E-05	1.13E-05	1.16E-05	1.06E-05	1.10E-05	8.48E-06	7.64E-06	
6.91E-06	7.51E-06	8.65E-06	9.04E-06	9.31E-06	1.00E-05	1.01E-05	1.01E-05	8.30E-06	9.30E-06	7.38E-06	7.06E-06	
1.60E-05	1.62E-05	1.55E-05	1.61E-05	1.66E-05	1.68E-05	1.62E-05	1.50E-05	1.46E-05	1.58E-05	1.32E-05	1.18E-05	
3.37E-05	2.87E-05	3.14E-05	2.98E-05	3.21E-05	3.07E-05	3.34E-05	3.10E-05	3.10E-05	2.53E-05	2.42E-05	2.18E-05	
7.47E-05	7.45E-05	7.59E-05	7.50E-05	7.48E-05	7.34E-05	7.09E-05	6.86E-05	6.44E-05	5.93E-05	5.26E-05	4.80E-05	
1.21E-05	9.98E-06	1.12E-05	1.08E-05	1.03E-05	1.08E-05	1.14E-05	1.20E-05	1.21E-05	1.09E-05	1.11E-05	9.52E-06	
4.39E-06	5.84E-06	5.22E-06	6.31E-06	6.57E-06	7.10E-06	6.89E-06	7.54E-06	9.60E-06	6.25E-06	5.52E-06	4.60E-06	
2.61E-05	2.67E-05	2.60E-05	2.64E-05	2.75E-05	2.69E-05	2.60E-05	2.55E-05	2.39E-05	2.18E-05	1.99E-05	1.84E-05	
2.70E-05	2.71E-05	2.75E-05	2.76E-05	2.73E-05	2.71E-05	2.64E-05	2.60E-05	2.42E-05	2.25E-05	2.02E-05	1.90E-05	
1.15E-05	1.22E-05	1.25E-05	1.30E-05	1.31E-05	1.34E-05	1.30E-05	1.32E-05	1.29E-05	1.20E-05	1.10E-05	1.03E-05	
6.96E-05	6.99E-05	7.10E-05	7.10E-05	7.07E-05	6.96E-05	6.76E-05	6.55E-05	6.03E-05	5.58E-05	4.95E-05	4.51E-05	
6.88E-05	6.90E-05	6.96E-05	6.97E-05	6.90E-05	6.83E-05	6.66E-05	6.44E-05	5.95E-05	5.57E-05	4.92E-05	4.51E-05	
2.38E-05	2.46E-05	2.59E-05	2.63E-05	2.63E-05	2.60E-05	2.51E-05	2.42E-05	2.20E-05	2.03E-05	1.81E-05	1.67E-05	
6.30E-05	6.40E-05	6.51E-05	6.60E-05	6.62E-05	6.55E-05	6.39E-05	6.17E-05	5.63E-05	5.18E-05	4.63E-05	4.37E-05	
7.40E-05	7.39E-05	7.57E-05	7.58E-05	7.56E-05	7.42E-05	7.24E-05	6.99E-05	6.47E-05	5.98E-05	5.26E-05	4.83E-05	
1.49E-04	1.51E-04	1.54E-04	1.52E-04	1.50E-04	1.48E-04	1.45E-04	1.39E-04	1.28E-04	1.19E-04	1.04E-04	9.32E-05	
1.40E-04	1.41E-04	1.43E-04	1.42E-04	1.41E-04	1.39E-04	1.35E-04	1.30E-04	1.19E-04	1.10E-04	9.72E-05	8.84E-05	
4.92E-05	4.95E-05	4.98E-05	5.00E-05	4.97E-05	4.90E-05	4.83E-05	4.69E-05	4.27E-05	4.06E-05	3.55E-05	3.24E-05	
2.17E-05	2.19E-05	2.24E-05	2.37E-05	2.24E-05	2.16E-05	2.26E-05	2.23E-05	2.04E-05	1.85E-05	1.73E-05	1.64E-05	
1.63E-05	1.68E-05	1.76E-05	1.84E-05	1.80E-05	1.85E-05	1.82E-05	1.80E-05	1.64E-05	1.59E-05	1.38E-05	1.30E-05	
1.49E-05	1.15E-05	1.33E-05	1.58E-05	1.54E-05	1.63E-05	1.52E-05	1.70E-05	1.35E-05	1.18E-05	1.38E-05	1.34E-05	
3.89E-05	3.86E-05	4.01E-05	4.02E-05	4.08E-05	3.96E-05	4.08E-05	3.84E-05	3.55E-05	2.98E-05	2.76E-05	2.51E-05	
1.66E-05	1.69E-05	1.79E-05	1.81E-05	1.81E-05	1.84E-05	1.82E-05	1.78E-05	1.61E-05	1.49E-05	1.37E-05	1.28E-05	
1.59E-05	1.61E-05	1.69E-05	1.76E-05	1.75E-05	1.74E-05	1.74E-05	1.71E-05	1.62E-05	1.52E-05	1.36E-05	1.27E-05	
2.07E-05	2.12E-05	2.14E-05	2.15E-05	2.11E-05	2.10E-05	2.07E-05	2.03E-05	1.96E-05	1.80E-05	1.65E-05	1.54E-05	
7.08E-02	7.18E-02	7.15E-02	6.87E-02	6.58E-02	6.37E-02	6.04E-02	5.80E-02	5.35E-02	5.06E-02	4.73E-02	4.55E-02	
4.76E-05	4.82E-05	4.91E-05	4.92E-05	4.93E-05	4.84E-05	4.78E-05	4.64E-05	4.28E-05	3.98E-05	3.53E-05	3.23E-05	
4.71E-05	4.74E-05	4.84E-05	4.85E-05	4.81E-05	4.79E-05	4.68E-05	4.52E-05	4.19E-05	3.93E-05	3.51E-05	3.20E-05	
1.67E-05	1.76E-05	1.76E-05	1.75E-05	1.82E-05	1.82E-05	1.76E-05	1.73E-05	1.68E-05	1.56E-05	1.37E-05	1.29E-05	
1.84E-05	1.90E-05	2.02E-05	1.93E-05	1.96E-05	1.97E-05	2.01E-05	2.00E-05	1.91E-05	1.67E-05	1.46E-05	1.44E-05	
5.44E-06	7.26E-06	1.11E-05	1.49E-05	1.86E-05	2.21E-05	2.89E-05	3.51E-05	4.86E-05	6.05E-05	8.03E-05	9.75E-05	
3.79E-05	3.70E-05	3.64E-05	3.59E-05	3.52E-05	3.46E-05	3.35E-05	3.23E-05	2.97E-05	2.74E-05	2.38E-05	2.11E-05	
3.64E-05	3.49E-05	3.47E-05	3.41E-05	3.35E-05	3.29E-05	3.19E-05	3.07E-05	2.83E-05	2.61E-05	2.27E-05	2.01E-05	

Table 3-2. Source organ residence times for  $^{99m}\text{Tc}$ -DMSA in a newborn.

Source organ	Residence time (h)
Bladder contents	0.22
Heart contents	0.10
Kidneys	2.88
Liver	0.40
Lungs	0.15
Spleen	0.10
Rest of body	5.25

Table 3-3. Internal dosimetry results and tissue weighting factors for the renal function case study.

Target	Organ equivalent dose (mSv / MBq)	$w_T$	Weighted dose (mSv/MBq)
Ovaries	6.93E-02	0.25	1.73E-02
Breast	2.04E-02	0.15	3.06E-03
Active Marrow	5.11E-02	0.12	6.13E-03
Lung	4.62E-02	0.12	5.55E-03
Thyroid	2.45E-02	0.03	7.34E-04
Endosteum	4.66E-02	0.03	1.40E-03
Remainder	5.75E-02	0.30	1.72E-02

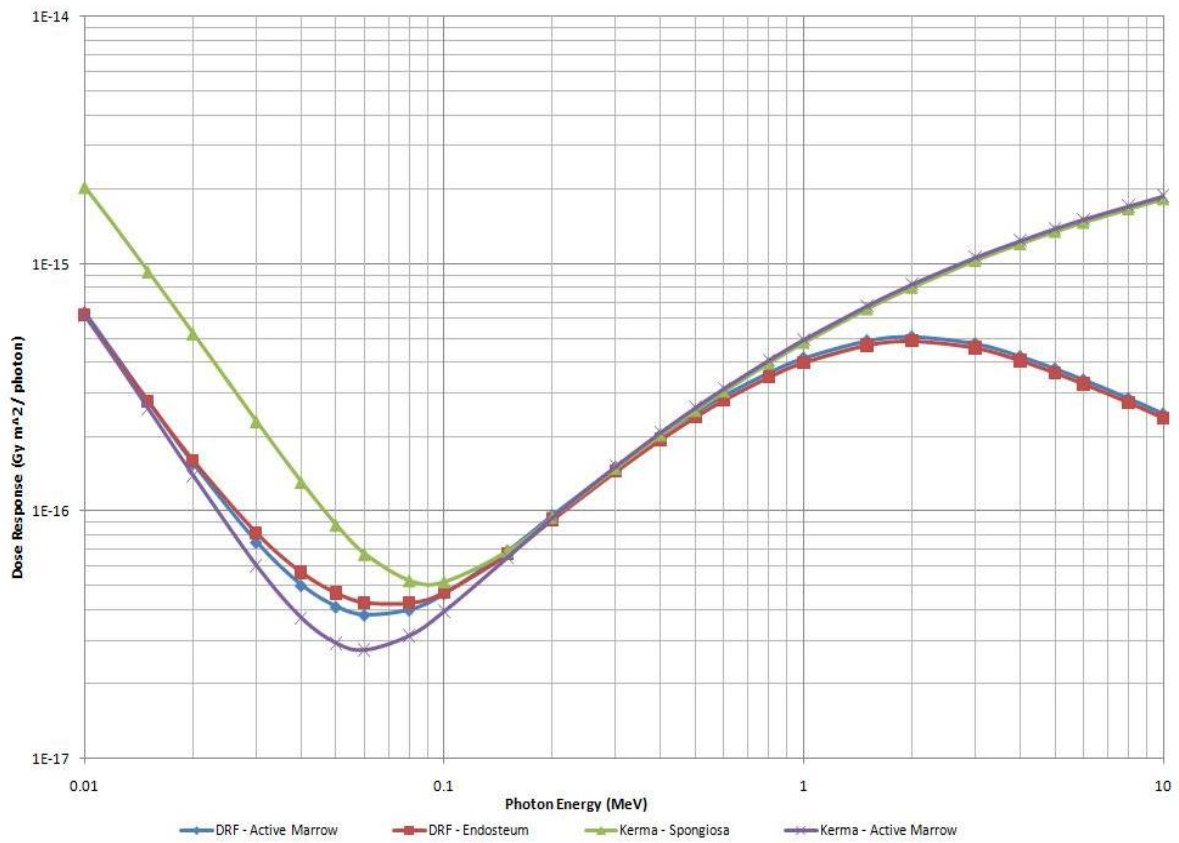
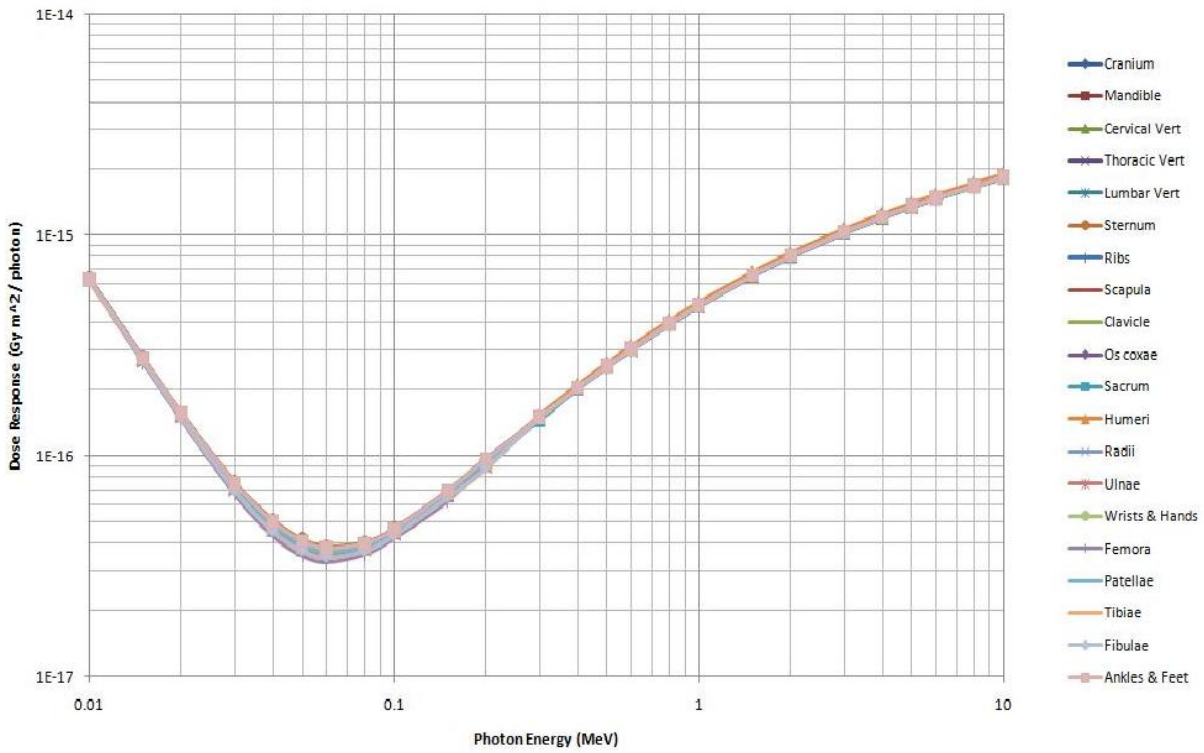
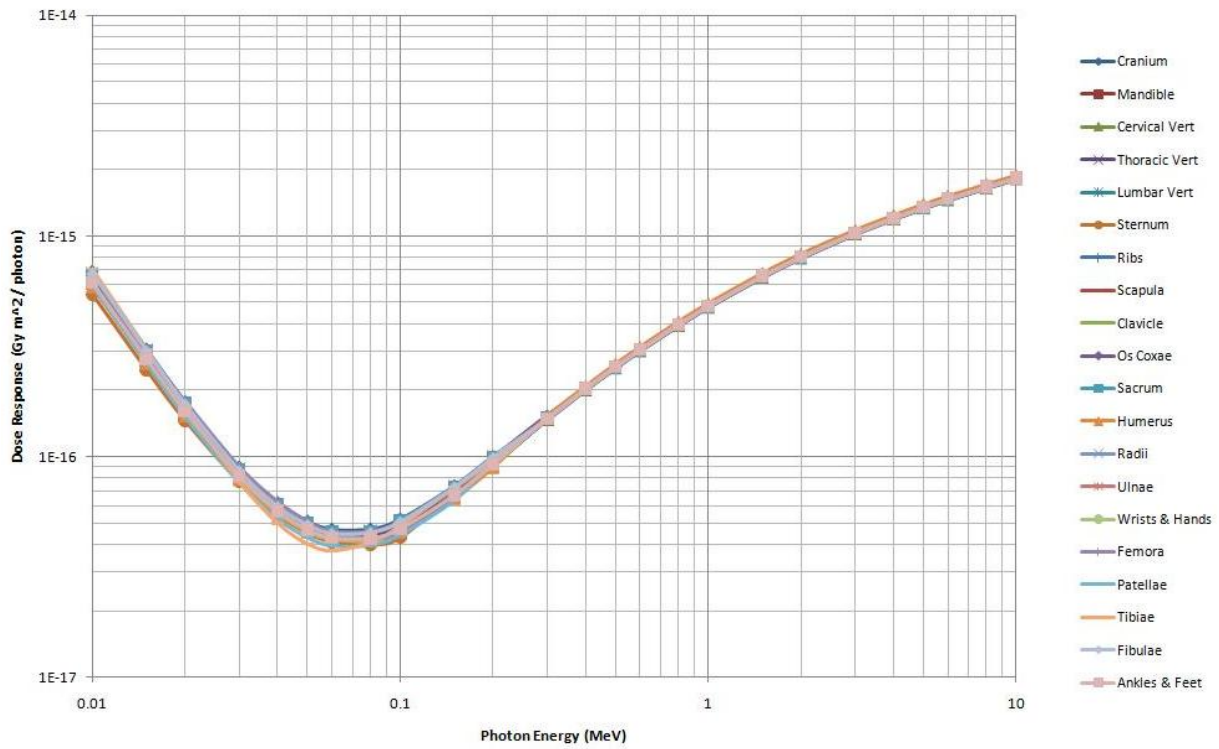


Figure 3-1. Dose response functions for active bone marrow and bone endosteum targets and kerma response functions for spongiosa and active bone marrow targets for the mandible.



A



B

Figure 3-2. Skeletal dose response functions for all bone sites. A) Active bone marrow target. B) Bone endosteum target.

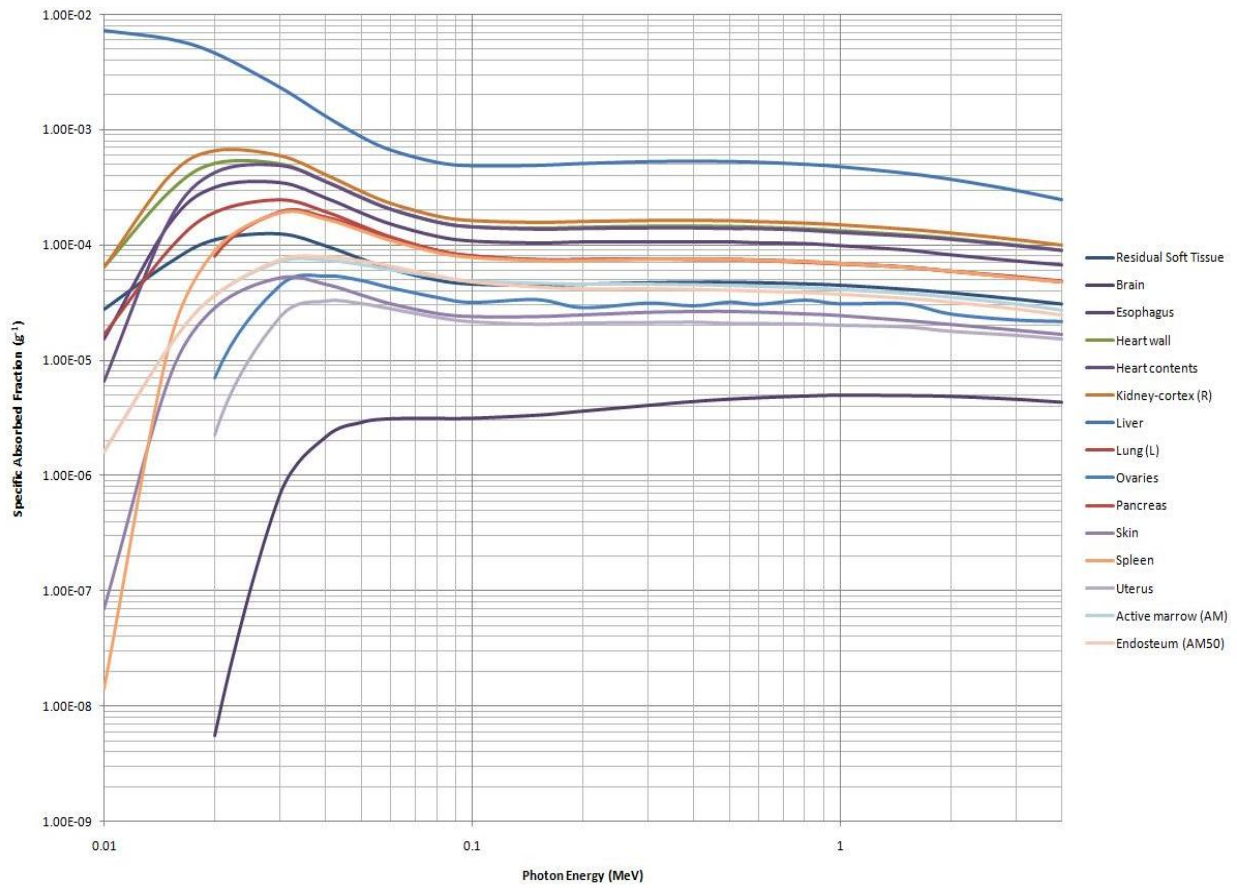


Figure 3-3. Specific absorbed fractions to selected target tissues from the liver source in the female UF newborn hybrid phantom.

## CHAPTER 4 DISCUSSION

### **ORNL Dose Response Functions**

During the development of the ORNL series of phantoms, skeletal DRFs were calculated and implemented, and these DRFs were calculated based on Equation 2-1. There were two distinct differences between the UF and ORNL methods of creating skeletal DRFs. The first difference was that ORNL used chord-length distributions of trabeculae and marrow cavities to obtain electron AFs (9) while UF actually performed detailed 3D radiation transport on the microstructure using EGSnrc. The second difference was that the UF skeletal DRFs were calculated based on data specific to the newborn phantom while the ORNL data was based on a 44 year old male and applied to *all* phantoms. One large difference between newborn and adult microstructure is that the newborn has almost no inactive marrow. This difference cannot be ignored, so age-dependent DRFs are needed. Immediately it could be seen that the UF DRFs utilized more detailed physics modeling and were more specific to the phantom of interest.

Three bone sites from the ORNL DRF data were selected for comparison and were chosen to be the cervical vertebra, lumbar vertebra, and ribs. The target was chosen to be AM. The UF and ORNL DRFs for those bone sites and AM target along with the percent difference between them can be seen in Table 4-1. The average absolute percent difference was found to be ~11%. At intermediate incident photon energies, the DRFs were found to be relatively close in agreement, but they tended to diverge at higher energies and at those energies where the DRF ceased to decline and began to increase. A graphical depiction of this comparison can be seen in Figure 4-1. The difference between these DRFs can be attributed to those reasons previously discussed: superior physics and anatomical specificity for the UF calculation of new skeletal DRFs.

## ORNL Newborn Specific Absorbed Fractions

The SAF data set reported by ORNL includes combinations of 56 source organs, 35 target organs, and 12 photon energies (27). So, it was evident at first sight that the SAF data produced for the UF newborn hybrid phantom was more comprehensive than the ORNL data with 61 source organs for the female, 63 source organs for the male, 60 target organs for the female, 62 target organs for the male, and 21 photon energies for both. Another advantage of the UF data was that it considered gender dependency more than ORNL. There are slight structure differences between the male and female phantoms which have the ability to perturb the photon fluence for certain source organ and photon energy combinations. The ORNL newborn stylized phantom is a hermaphrodite and so does not take into account the difference in photon interactions between male and female, however slight.

For this comparison, a representative source organ was chosen to compare the SAFs calculated using the UF newborn hybrid phantom to those obtained using the ORNL newborn stylized phantom. The source organ was chosen to be the liver, as before, for the female phantom. Several target tissues were arbitrarily selected for comparison. SAF data for the ORNL newborn stylized phantom were taken from ORNL/TM-8381/V6 (27). The percent difference between the UF newborn female hybrid phantom and the ORNL newborn stylized phantom SAFs for the liver source can be seen in Table 4-2. The percent difference was calculated with respect to the ORNL phantom, so a positive percent difference means that the UF phantom showed a greater SAF for that particular source-target-energy combination.

Several values were removed from Table 4-2 for one of two reasons. The first scenario in which data was removed from this table was if both the UF and ORNL SAFs were found to be effectively zero. Mathematically, even though both SAFs were found to be the same, this similarity produced no meaningful information. It simply meant that the emitted photons were

not of great enough energy to reach the target organ of interest. The second scenario in which data was removed from the table was if both SAFs were reported to be greater than zero, but the ORNL SAF was so close to zero that a percent difference created a very large percent difference. For example,  $\Phi(Spleen \leftarrow Liver, 0.01 MeV)$  was found to be  $1.42 \times 10^{-8} g^{-1}$  for the UF phantom and  $2.51 \times 10^{-12} g^{-1}$  for the ORNL phantom, producing a percent difference of 566354%. Obviously, this was not a meaningful result. The ORNL SAF was so close to zero that it could be considered effectively zero.

It was found from this comparison that while the UF SAFs were generally of the same order of magnitude as the ORNL SAFs, there was still a significant change in many of the SAFs. The overall average absolute difference between the SAFs calculated for the UF and ORNL phantoms was found to be ~74%.

Once it was proven that there was a fairly significant difference between the SAFs based on the stylized and hybrid phantoms, it was necessary to evaluate whether this new set of SAFs was an improvement upon the old SAFs. In view of the previous discussions on the anatomical accuracy of the new UF hybrid phantoms, it was surmised that the SAFs calculated based on these phantoms were an improvement upon those based on the ORNL stylized phantoms. Not only are the SAFs more accurate because the anatomy in the hybrid phantoms more closely resembles real human anatomy, but the phantoms can easily be extended to different body morphometries for internal dose assessment of non-50%ile individuals.

### **Renal Function Case Study**

The results of the renal function dosimetry case study were compared to the dosimetry from a previous study which used the ORNL newborn stylized phantom (20). The comparison can be seen in Table 4-3. While the electron dosimetry was admittedly rough,  $^{99m}Tc$  is

principally a single photon emitter, so the electron component of the total dose is a relatively small fraction of the whole. Therefore, it was not completely inappropriate to compare the results of the comprehensive photon dosimetry and rough electron dosimetry of the UF newborn female hybrid phantom with the ORNL newborn stylized phantom. It was found that there were fairly significant differences in the estimate dose to individual organs but not a large difference in the whole-body effective dose.

Overall, this analysis showed that it is relatively straight forward to calculate the individual organ equivalent doses and whole-body effective dose with the SAF data generated from this study. This data could be applied to any radionuclide and therefore any nuclear medicine imaging, or even therapy, procedure. Incorporated into a software package, dose estimates could be provided very quickly and possibly recorded for every nuclear medicine imaging procedure. With vast records of dose estimates, patients could be tracked throughout their lives, and updated radiation risk estimates could be provided.

Another application of these SAFs could be imaging optimization. With quick estimates of whole-body effective dose, image quality could be indexed against administered activity and effective dose. The analysis of these results could yield imaging protocols which maximize the image quality and minimize the absorbed dose.

Table 4-1. Percent difference between the UF newborn female hybrid phantom and the ORNL adult stylized phantom skeletal dose response functions for selected bone sites (9).

Photon energy (MeV)	UF newborn hybrid phantom			ORNL adult male			Difference		
	Cervical vertebra	Lumbar vertebra	Ribs	Cervical vertebra	Lumbar vertebra	Ribs	Cervical vertebra	Lumbar vertebra	Ribs
0.01	6.32E-16	6.32E-16	6.33E-16	6.16E-16	6.14E-16	6.12E-16	3%	3%	3%
0.015	2.76E-16	2.75E-16	2.76E-16	2.62E-16	2.61E-16	2.59E-16	5%	6%	7%
0.02	1.55E-16	1.55E-16	1.55E-16	1.45E-16	1.43E-16	1.41E-16	7%	8%	10%
0.03	7.44E-17	7.42E-17	7.45E-17	6.60E-17	6.44E-17	6.29E-17	13%	15%	19%
0.04	4.98E-17	4.95E-17	4.99E-17	4.27E-17	4.11E-17	3.99E-17	17%	21%	25%
0.05	4.07E-17	4.05E-17	4.08E-17	3.45E-17	3.31E-17	3.20E-17	18%	22%	27%
0.06	3.77E-17	3.76E-17	3.79E-17	3.26E-17	3.11E-17	3.01E-17	16%	21%	26%
0.08	3.97E-17	3.96E-17	3.97E-17	3.58E-17	3.45E-17	3.36E-17	11%	15%	18%
0.1	4.61E-17	4.61E-17	4.61E-17	4.33E-17	4.22E-17	4.14E-17	6%	9%	11%
0.15	6.90E-17	6.91E-17	6.88E-17	6.83E-17	6.74E-17	6.68E-17	1%	3%	3%
0.2	9.61E-17	9.63E-17	9.56E-17	9.63E-17	9.57E-17	9.52E-17	0%	1%	0%
0.3	1.48E-16	1.48E-16	1.49E-16	1.54E-16	1.54E-16	1.53E-16	-4%	-4%	-3%
0.4	2.01E-16	2.02E-16	2.03E-16	2.12E-16	2.10E-16	2.10E-16	-5%	-4%	-3%
0.5	2.53E-16	2.54E-16	2.56E-16	2.67E-16	2.66E-16	2.65E-16	-5%	-5%	-4%
0.6	3.02E-16	3.03E-16	3.05E-16	3.20E-16	3.19E-16	3.17E-16	-6%	-5%	-4%
0.8	3.94E-16	3.95E-16	3.97E-16	4.17E-16	4.15E-16	4.14E-16	-6%	-5%	-4%
1	4.76E-16	4.78E-16	4.81E-16	5.06E-16	5.03E-16	5.01E-16	-6%	-5%	-4%
1.5	6.52E-16	6.54E-16	6.59E-16	6.95E-16	6.91E-16	6.89E-16	-6%	-5%	-4%
2	7.97E-16	7.99E-16	8.05E-16	8.56E-16	8.50E-16	8.47E-16	-7%	-6%	-5%
3	1.02E-15	1.03E-15	1.03E-15	1.13E-15	1.12E-15	1.11E-15	-9%	-8%	-7%
4	1.20E-15	1.20E-15	1.21E-15	1.37E-15	1.37E-15	1.35E-15	-13%	-12%	-10%
5	1.34E-15	1.34E-15	1.35E-15	1.60E-15	1.59E-15	1.57E-15	-16%	-15%	-14%
6	1.46E-15	1.47E-15	1.47E-15	1.82E-15	1.80E-15	1.78E-15	-20%	-19%	-17%
8	1.66E-15	1.66E-15	1.67E-15	2.27E-15	2.23E-15	2.20E-15	-27%	-26%	-24%
10	1.82E-15	1.82E-15	1.83E-15	2.71E-15	2.66E-15	2.62E-15	-33%	-31%	-30%

Table 4-2. Difference between the UF newborn female hybrid phantom and the ORNL newborn stylized phantom SAFs for selected target organs for the liver source.

Target	Photon energy (MeV)											
	0.01	0.015	0.02	0.03	0.05	0.1	0.2	0.5	1	1.5	2	4
Adrenals	117%	36%	36%	32%	27%	25%	23%	27%	29%	26%	26%	30%
Urinary bladder wall	--	-53%	-64%	-36%	-38%	-30%	-29%	-27%	-27%	-28%	-28%	-32%
Endosteum	-90%	-85%	-83%	-79%	-70%	-39%	0%	8%	3%	4%	4%	-3%
Brain	--	--	657%	89%	109%	58%	74%	60%	48%	54%	58%	36%
Breasts	--	-33%	-5%	0%	0%	4%	9%	3%	3%	1%	-8%	-8%
Stomach wall	703%	133%	70%	44%	38%	35%	33%	32%	28%	28%	30%	38%
Small intestine wall	45%	37%	10%	-12%	-17%	-14%	-12%	-12%	-18%	-16%	-15%	-13%
Kidneys	311%	103%	49%	22%	9%	5%	3%	3%	6%	9%	10%	3%
Liver	-5%	-5%	-5%	-4%	-5%	-6%	-6%	-8%	-9%	-14%	-18%	-32%
Ovaries	--	-64%	-48%	-41%	-28%	-28%	-29%	-18%	-12%	-11%	-25%	-19%
Pancreas	--	-95%	-83%	-65%	-52%	-51%	-53%	-54%	-52%	-52%	-53%	-53%
Active marrow	-31%	6%	31%	63%	85%	94%	91%	75%	64%	63%	62%	54%
Skin	-94%	-44%	-18%	4%	16%	13%	4%	2%	-1%	-5%	-6%	-6%
Spleen	--	1388%	290%	96%	58%	50%	50%	46%	48%	53%	52%	40%
Thymus	--	2256%	446%	171%	118%	100%	83%	72%	85%	87%	90%	67%
Thyroid	--	--	1007%	163%	94%	75%	74%	73%	70%	61%	52%	61%
Gall bladder wall	2%	13%	7%	7%	7%	6%	8%	3%	2%	3%	2%	-2%
Heart wall	677%	169%	102%	73%	54%	49%	44%	45%	43%	44%	45%	46%
Uterus	--	-93%	-75%	-63%	-51%	-46%	-44%	-47%	-43%	-43%	-46%	-40%

Table 4-3. Dosimetry comparison between a previous dose estimation for the renal function case study and the dose estimation using the UF newborn hybrid phantom (20).

Target	Normalized dose (mSv / MBq)		Difference
	Previous study	UF hybrid	
Kidneys	2.000	1.518	-24%
Ovaries	0.037	0.069	87%
Endosteum	0.052	0.036	-30%
Active marrow	0.029	0.038	30%
Urinary bladder wall	0.052	0.067	30%
Whole-body effective dose	0.160	0.163	2%

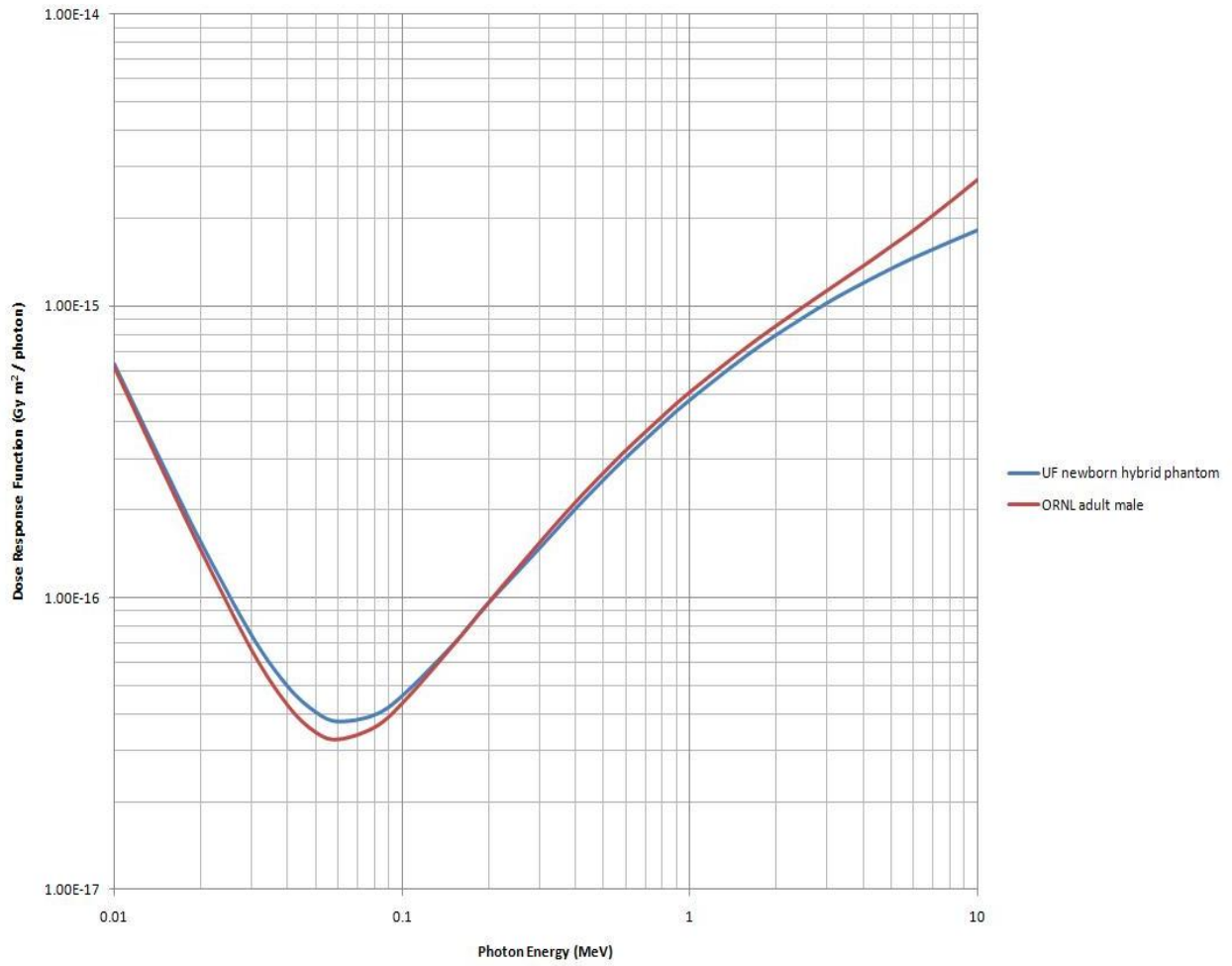


Figure 4-1. UF newborn hybrid phantom and ORNL adult male stylized phantom dose response functions for the cervical vertebra with AM as the target (9).

## CHAPTER 5 CONCLUSION

A recent study showed a considerable variability in the administered activity to pediatric patients undergoing nuclear medicine imaging procedures with a maximum variation of 8.5 and an average variation of 3 (28). This means that if a particular pediatric patient was scanned at one hospital, there was a chance that the child would receive up to 8.5 times the administered activity for the same procedure at a different institution. Obviously, in this scenario, one institution considers their administered activity sufficient to produce a quality image while another institution overdoses the child to potentially obtain the same result.

This example shows that there is a great need for accurate dosimetry in nuclear medicine imaging. How much activity is enough to produce the optimal quality image for this child? This question has not yet been answered, but to answer that question, high quality dosimetry methods are needed to analyze the dosing protocols. To date, the internal dosimetry parameters, SAFs, were taken from the ORNL series of stylized phantoms. As discussed previously, these phantoms are simply not anatomically accurate. They do not faithfully represent human anatomy in shape and sometimes position. In addition, the simple skeletal models do not take into account detailed radiation transport in the skeletal microstructure.

The UF hybrid series of phantoms possesses anatomical accuracy as well as an updated skeletal microstructure. In this study, the UF newborn hybrid phantoms were used to calculate a new set of SAFs for a wide range of source-target-energy combinations. These new SAFs were shown to be applicable for not only the renal function case study but for *any* nuclear medicine imaging procedure. The new SAFs were shown to differ significantly from the SAFs calculated by ORNL for their stylized newborn phantom. The comparison between these SAFs demonstrated the need to utilize the UF hybrid phantom series for internal dosimetry.

The application of this new set of SAFs to nuclear medicine imaging dosimetry is boundless provided accurate biokinetics and radionuclide information are available. The results of this study will be able to be used in the future by anyone when it is imbedded in a software program. Along with the newborn phantom, the rest of the UF hybrid phantom series will be included and will provide a complete internal dosimetry model that may be adopted by international governing bodies. So, this study has the capability of greatly contributing to the ever improving field of computational radiation dosimetry.

APPENDIX A  
SAMPLE FILES

**Sample Lattice File (Excerpt)**

```
1000 0 -200 lat=1 u=999 imp:p=1 imp:e=1 fill=0:345 0:211 0:715
 57 15588r 43 57 306r 43 57 34r 43 4r 57 302r 43 4r 57 31r
 43 6r 57 300r 43 6r 57 29r 43 7r 57 300r 43 7r 57 28r
 43 8r 57 298r 43 8r 57 28r 43 8r 57 298r 43 8r 57 28r
 43 9r 57 296r 43 9r 57 28r 43 9r 57 296r 43 9r 57 29r
```

...

**Sample Source Files (Excerpts)**

**Uniform Sampling Probability (Liver Source)**

```
si5 1 (25<1000[ 109 132 306]<1001) (25<1000[ 109 133 306]<1001)
(25<1000[ 109 134 306]<1001) (25<1000[ 108 126 307]<1001)
(25<1000[ 109 126 307]<1001) (25<1000[ 110 126 307]<1001)
(25<1000[ 108 127 307]<1001) (25<1000[ 109 127 307]<1001)
(25<1000[ 110 127 307]<1001) (25<1000[ 107 128 307]<1001)
```

...

```
(25<1000[ 150 112 444]<1001) (25<1000[ 145 113 444]<1001)
(25<1000[ 146 113 444]<1001) (25<1000[ 147 113 444]<1001)
(25<1000[ 148 113 444]<1001) (25<1000[ 149 113 444]<1001)
(25<1000[ 146 114 444]<1001) (25<1000[ 147 114 444]<1001)
(25<1000[ 148 114 444]<1001)
```

```
sp5 1 427350r
```

**Non-Uniform Sampling Probability (AM Source)**

```
si5 s d201 d202 d203 d204 d205 d206 d207 d208 d209 d210
d211 d212 d213 d214 d215 d216 d217 d218 d219 d220
d221 d222 d223 d224 d225 d226 d227 d228 d229 d230
d231 d232 d233 d234
```

```
sp5 0.2412 0.0433 0.0373 0.0516 0.0470 0.0051 0.1628
0.0323 0.0122 0.0631 0.0188 0.0212 0.0045 0.0045
0.0166 0.0036 0.0017 0.0065 0.0086 0.0020 0.0044
0.0242 0.0346 0.0103 0.0164 0.0286 0.0013 0.0246
0.0094 0.0151 0.0033 0.0015 0.0050 0.0375
```

```
si201 1 (201<1000[ 173 53 569]<1001) (201<1000[ 174 53 569]<1001)
(201<1000[ 171 54 569]<1001) (201<1000[ 172 54 569]<1001)
(201<1000[ 173 54 569]<1001) (201<1000[ 174 54 569]<1001)
```

...

```
(201<1000[ 156 156 709]<1001) (201<1000[ 156 157 709]<1001)
(201<1000[ 157 158 709]<1001)
```

```
sp201 1 166946r
```

...

```
si234 1 (234<1000[ 56 110 255]<1001) (234<1000[ 57 110 255]<1001)
(234<1000[ 289 110 255]<1001) (234<1000[ 290 110 255]<1001)
(234<1000[ 56 111 255]<1001) (234<1000[ 57 111 255]<1001)
```

...

(234<1000[ 56 104 322]<1001) (234<1000[ 290 104 322]<1001)  
(234<1000[ 291 104 322]<1001) (234<1000[ 292 104 322]<1001)  
sp234 1 7437r

### Sample MCNPX Input File (Excerpt)

#### Female Newborn Phantom – 4 MeV Photon Energy – Liver Source

```
c -----  
c -----  
c -----  
c  
c           UFH Newborn Female  
c           Mike Wayson  
c           Contributions from Choonsik Lee  
c           The University of Florida  
c           Complete Dosimetry Characterization (SAFs)  
c           ALRADS Research Group  
c  
c -----  
c -----  
c -----  
c  
read file=nbfp.e.lat noecho  
1001 0 -100 fill=999 imp:p=1 imp:e=1    $ Surrounding Box  
c  
c -----  
c -----  
c  
c           Body composition and density  
c  
c -----  
c -----  
c  
1  1 -1.02 -70 u=1  imp:p=1 imp:e=1 vol=2085.280 $ Residual Soft Tissue  
2  1 -1.02 -70 u=2  imp:p=1 imp:e=1 vol=2.899  $ Adrenal (L)  
3  1 -1.02 -70 u=3  imp:p=1 imp:e=1 vol=2.880  $ Adrenal (R)  
4  1 -1.02 -70 u=4  imp:p=1 imp:e=1 vol=307.483 $ Brain  
5  1 -1.02 -70 u=5  imp:p=1 imp:e=1 vol=0.043  $ Breast  
6  1 -1.02 -70 u=6  imp:p=1 imp:e=1 vol=0.355  $ Bronchi  
7  1 -1.02 -70 u=7  imp:p=1 imp:e=1 vol=6.710  $ Right Colon W  
8  1 -1.02 -70 u=8  imp:p=1 imp:e=1 vol=15.123 $ Right Colon C  
9  1 -1.02 -70 u=9  imp:p=1 imp:e=1 vol=0.963  $ Ears  
10 1 -1.02 -70 u=10 imp:p=1 imp:e=1 vol=1.900  $ Esophagus  
11 1 -1.02 -70 u=11 imp:p=1 imp:e=1 vol=0.234  $ External nose  
12 1 -1.02 -70 u=12 imp:p=1 imp:e=1 vol=5.752  $ Eye balls  
13 1 -1.02 -70 u=13 imp:p=1 imp:e=1 vol=0.481  $ Gall Bladder W  
14 1 -1.02 -70 u=14 imp:p=1 imp:e=1 vol=2.720  $ Gall Bladder C  
15 1 -1.02 -70 u=15 imp:p=1 imp:e=1 vol=19.134 $ Heart W  
16 1 -1.02 -70 u=16 imp:p=1 imp:e=1 vol=5.647  $ Heart C  
17 1 -1.02 -70 u=17 imp:p=1 imp:e=1 vol=8.908  $ Kidney-cortex (L)  
18 1 -1.02 -70 u=18 imp:p=1 imp:e=1 vol=8.911  $ Kidney-cortex (R)  
19 1 -1.02 -70 u=19 imp:p=1 imp:e=1 vol=3.180  $ Kidney-medulla (L)  
20 1 -1.02 -70 u=20 imp:p=1 imp:e=1 vol=3.179  $ Kidney-medulla (R)  
21 1 -1.02 -70 u=21 imp:p=1 imp:e=1 vol=0.637  $ Kidney-pelvis (L)
```

22 1 -1.02 -70 u=22 imp:p=1 imp:e=1 vol=0.636 \$ Kidney-pelvis (R)  
23 1 -1.02 -70 u=23 imp:p=1 imp:e=1 vol=1.216 \$ Larynx  
24 1 -1.02 -70 u=24 imp:p=1 imp:e=1 vol=0.122 \$ Lens  
25 1 -1.02 -70 u=25 imp:p=1 imp:e=1 vol=124.545 \$ Liver  
26 2 -0.62 -70 u=26 imp:p=1 imp:e=1 vol=46.428 \$ Lung (L)  
27 2 -0.62 -70 u=27 imp:p=1 imp:e=1 vol=50.660 \$ Lung (R)  
28 1 -1.02 -70 u=28 imp:p=1 imp:e=1 vol=0.080 \$ Nasal layer (anterior)  
29 1 -1.02 -70 u=29 imp:p=1 imp:e=1 vol=0.715 \$ Nasal layer (posterior)  
30 1 -1.02 -70 u=30 imp:p=1 imp:e=1 vol=0.716 \$ Oral cavity layer  
31 1 -1.02 -70 u=31 imp:p=1 imp:e=1 vol=0.287 \$ Ovaries <--  
32 1 -1.02 -70 u=32 imp:p=1 imp:e=1 vol=5.791 \$ Pancreas  
c 33 1 -1.02 -70 u=33 imp:p=1 imp:e=1 vol=0.000 \$ Penis <--  
34 1 -1.02 -70 u=34 imp:p=1 imp:e=1 vol=0.277 \$ Pharynx  
35 1 -1.02 -70 u=35 imp:p=1 imp:e=1 vol=0.096 \$ Pituitary Gland  
c 36 1 -1.02 -70 u=36 imp:p=1 imp:e=1 vol=0.000 \$ Prostate <--  
37 1 -1.02 -70 u=37 imp:p=1 imp:e=1 vol=2.917 \$ Rectosigmoid W  
38 1 -1.02 -70 u=38 imp:p=1 imp:e=1 vol=9.220 \$ Rectosigmoid C  
39 1 -1.02 -70 u=39 imp:p=1 imp:e=1 vol=3.393 \$ Salivary Glands (parotid)  
c 40 1 -1.02 -70 u=40 imp:p=1 imp:e=1 vol=0.000 \$ Scrotum <--  
41 1 -1.02 -70 u=41 imp:p=1 imp:e=1 vol=28.175 \$ SI W  
42 1 -1.02 -70 u=42 imp:p=1 imp:e=1 vol=30.330 \$ SI C  
43 1 -1.02 -70 u=43 imp:p=1 imp:e=1 vol=143.621 \$ Skin  
44 1 -1.02 -70 u=44 imp:p=1 imp:e=1 vol=6.099 \$ Spinal Cord  
45 1 -1.02 -70 u=45 imp:p=1 imp:e=1 vol=9.103 \$ Spleen  
46 1 -1.02 -70 u=46 imp:p=1 imp:e=1 vol=6.767 \$ Stomach W  
47 1 -1.02 -70 u=47 imp:p=1 imp:e=1 vol=24.555 \$ Stomach C  
c 48 1 -1.02 -70 u=48 imp:p=1 imp:e=1 vol=0.000 \$ Testes <--  
49 1 -1.02 -70 u=49 imp:p=1 imp:e=1 vol=12.122 \$ Thymus  
50 1 -1.02 -70 u=50 imp:p=1 imp:e=1 vol=1.227 \$ Thyroid  
51 1 -1.02 -70 u=51 imp:p=1 imp:e=1 vol=3.340 \$ Tongue  
52 1 -1.02 -70 u=52 imp:p=1 imp:e=1 vol=0.098 \$ Tonsil  
53 1 -1.02 -70 u=53 imp:p=1 imp:e=1 vol=0.475 \$ Trachea  
54 1 -1.02 -70 u=54 imp:p=1 imp:e=1 vol=3.814 \$ Urinary bladder W  
55 1 -1.02 -70 u=55 imp:p=1 imp:e=1 vol=9.947 \$ Urinary bladder C  
56 1 -1.02 -70 u=56 imp:p=1 imp:e=1 vol=3.775 \$ Uterus <--  
57 4 -0.0012 -70 u=57 imp:p=1 imp:e=1 vol=1.540 \$ Air (in body)  
58 1 -1.02 -70 u=58 imp:p=1 imp:e=1 vol=6.787 \$ Left Colon W  
59 1 -1.02 -70 u=59 imp:p=1 imp:e=1 vol=18.398 \$ Left Colon C  
60 1 -1.02 -70 u=60 imp:p=1 imp:e=1 vol=1.740 \$ Salivary Glands (submaxillary)  
61 1 -1.02 -70 u=61 imp:p=1 imp:e=1 vol=0.676 \$ Salivary Glands (sublingual)  
101 5 -1.10 -70 u=101 imp:p=1 imp:e=1 vol=35.079 \$ c-Cranium  
102 5 -1.10 -70 u=102 imp:p=1 imp:e=1 vol=2.453 \$ c-Mandible  
103 5 -1.10 -70 u=103 imp:p=1 imp:e=1 vol=2.486 \$ c-Scapulae  
104 5 -1.10 -70 u=104 imp:p=1 imp:e=1 vol=1.215 \$ c-Clavicles  
105 5 -1.10 -70 u=105 imp:p=1 imp:e=1 vol=1.432 \$ c-Sternum  
106 5 -1.10 -70 u=106 imp:p=1 imp:e=1 vol=4.073 \$ c-Ribs  
107 5 -1.10 -70 u=107 imp:p=1 imp:e=1 vol=3.832 \$ c-Vertebrae-C  
108 5 -1.10 -70 u=108 imp:p=1 imp:e=1 vol=7.208 \$ c-Vertebrae-T  
109 5 -1.10 -70 u=109 imp:p=1 imp:e=1 vol=3.879 \$ c-Vertebrae-L  
110 5 -1.10 -70 u=110 imp:p=1 imp:e=1 vol=1.766 \$ c-Sacrum  
111 5 -1.10 -70 u=111 imp:p=1 imp:e=1 vol=5.351 \$ c-Os Coxae  
112 5 -1.10 -70 u=112 imp:p=1 imp:e=1 vol=2.451 \$ c-Femora-p  
113 5 -1.10 -70 u=113 imp:p=1 imp:e=1 vol=2.158 \$ c-Femora-d  
114 5 -1.10 -70 u=114 imp:p=1 imp:e=1 vol=1.601 \$ c-Tibiae-p  
115 5 -1.10 -70 u=115 imp:p=1 imp:e=1 vol=1.507 \$ c-Tibiae-d  
116 5 -1.10 -70 u=116 imp:p=1 imp:e=1 vol=0.636 \$ c-Fibulae-p

117 5 -1.10 -70 u=117 imp:p=1 imp:e=1 vol=0.842 \$ c-Fibulae-d  
118 5 -1.10 -70 u=118 imp:p=1 imp:e=1 vol=0.129 \$ c-Patellae  
119 5 -1.10 -70 u=119 imp:p=1 imp:e=1 vol=3.752 \$ c-Feet  
120 5 -1.10 -70 u=120 imp:p=1 imp:e=1 vol=1.521 \$ c-Humera-p  
121 5 -1.10 -70 u=121 imp:p=1 imp:e=1 vol=1.790 \$ c-Humera-d  
122 5 -1.10 -70 u=122 imp:p=1 imp:e=1 vol=0.595 \$ c-Radii-p  
123 5 -1.10 -70 u=123 imp:p=1 imp:e=1 vol=0.839 \$ c-Radii-d  
124 5 -1.10 -70 u=124 imp:p=1 imp:e=1 vol=0.873 \$ c-Ulnae-p  
125 5 -1.10 -70 u=125 imp:p=1 imp:e=1 vol=0.906 \$ c-Ulnae-d  
126 5 -1.10 -70 u=126 imp:p=1 imp:e=1 vol=3.803 \$ c-Hands  
127 5 -1.10 -70 u=127 imp:p=1 imp:e=1 vol=10.209 \$ c-Cranial Cap  
128 5 -1.10 -70 u=128 imp:p=1 imp:e=1 vol=10.531 \$ c-Costal cartilage of ribs  
129 5 -1.10 -70 u=129 imp:p=1 imp:e=1 vol=0.204 \$ c-Cervical Discs  
130 5 -1.10 -70 u=130 imp:p=1 imp:e=1 vol=0.690 \$ c-Thoracic Discs  
131 5 -1.10 -70 u=131 imp:p=1 imp:e=1 vol=0.474 \$ c-Lumbar Discs  
151 3 -1.65 -70 u=151 imp:p=1 imp:e=1 vol=12.848 \$ Cranium  
152 3 -1.65 -70 u=152 imp:p=1 imp:e=1 vol=1.017 \$ Mandible  
153 3 -1.65 -70 u=153 imp:p=1 imp:e=1 vol=1.458 \$ Scapulae  
154 3 -1.65 -70 u=154 imp:p=1 imp:e=1 vol=0.552 \$ Clavicles  
155 3 -1.65 -70 u=155 imp:p=1 imp:e=1 vol=0.105 \$ Sternum  
156 3 -1.65 -70 u=156 imp:p=1 imp:e=1 vol=3.700 \$ Ribs  
157 3 -1.65 -70 u=157 imp:p=1 imp:e=1 vol=2.204 \$ Vertebrae-C  
158 3 -1.65 -70 u=158 imp:p=1 imp:e=1 vol=5.114 \$ Vertebrae-T  
159 3 -1.65 -70 u=159 imp:p=1 imp:e=1 vol=1.623 \$ Vertebrae-L  
160 3 -1.65 -70 u=160 imp:p=1 imp:e=1 vol=0.672 \$ Sacrum  
161 3 -1.65 -70 u=161 imp:p=1 imp:e=1 vol=3.724 \$ Os Coxae  
162 3 -1.65 -70 u=162 imp:p=1 imp:e=1 vol=0.398 \$ Femora-proximal  
163 3 -1.65 -70 u=163 imp:p=1 imp:e=1 vol=1.911 \$ Femora-upper shaft  
164 3 -1.65 -70 u=164 imp:p=1 imp:e=1 vol=3.001 \$ Femora-lower shaft  
165 3 -1.65 -70 u=165 imp:p=1 imp:e=1 vol=0.326 \$ Femora-distal  
166 3 -1.65 -70 u=166 imp:p=1 imp:e=1 vol=0.325 \$ Tibiae-proximal  
167 3 -1.65 -70 u=167 imp:p=1 imp:e=1 vol=2.211 \$ Tibiae-shaft  
168 3 -1.65 -70 u=168 imp:p=1 imp:e=1 vol=0.170 \$ Tibiae-distal  
169 3 -1.65 -70 u=169 imp:p=1 imp:e=1 vol=0.030 \$ Fibulae-proximal  
170 3 -1.65 -70 u=170 imp:p=1 imp:e=1 vol=0.618 \$ Fibulae-shaft  
171 3 -1.65 -70 u=171 imp:p=1 imp:e=1 vol=0.047 \$ Fibulae-distal  
172 3 -1.65 -70 u=172 imp:p=1 imp:e=1 vol=0.033 \$ Patellae  
173 3 -1.65 -70 u=173 imp:p=1 imp:e=1 vol=0.738 \$ Ankles and Feet  
174 3 -1.65 -70 u=174 imp:p=1 imp:e=1 vol=0.251 \$ Humera-proximal  
175 3 -1.65 -70 u=175 imp:p=1 imp:e=1 vol=0.957 \$ Humera-upper shaft  
176 3 -1.65 -70 u=176 imp:p=1 imp:e=1 vol=0.916 \$ Humera-lower shaft  
177 3 -1.65 -70 u=177 imp:p=1 imp:e=1 vol=0.154 \$ Humera-distal  
178 3 -1.65 -70 u=178 imp:p=1 imp:e=1 vol=0.035 \$ Radii-proximal  
179 3 -1.65 -70 u=179 imp:p=1 imp:e=1 vol=0.615 \$ Radii-shaft  
180 3 -1.65 -70 u=180 imp:p=1 imp:e=1 vol=0.056 \$ Radii-distal  
181 3 -1.65 -70 u=181 imp:p=1 imp:e=1 vol=0.119 \$ Ulnae-proximal  
182 3 -1.65 -70 u=182 imp:p=1 imp:e=1 vol=0.790 \$ Ulnae-shaft  
183 3 -1.65 -70 u=183 imp:p=1 imp:e=1 vol=0.062 \$ Ulnae-distal  
184 3 -1.65 -70 u=184 imp:p=1 imp:e=1 vol=0.494 \$ Wrists and Hands  
c 185 3 -1.65 -70 u=185 imp:p=1 imp:e=1 vol=0.000 \$ Teeth  
201 6 -1.33 -70 u=201 imp:p=1 imp:e=1 vol=48.654 \$ sp-Cranium  
202 6 -1.33 -70 u=202 imp:p=1 imp:e=1 vol=3.856 \$ sp-Mandible  
203 6 -1.33 -70 u=203 imp:p=1 imp:e=1 vol=3.007 \$ sp-Scapulae  
204 6 -1.33 -70 u=204 imp:p=1 imp:e=1 vol=1.135 \$ sp-Clavicles  
205 6 -1.33 -70 u=205 imp:p=1 imp:e=1 vol=0.455 \$ sp-Sternum  
206 6 -1.33 -70 u=206 imp:p=1 imp:e=1 vol=14.466 \$ sp-Ribs

```

207 6 -1.33 -70 u=207 imp:p=1 imp:e=1 vol=4.641 $ sp-Vertebrae-C
208 6 -1.33 -70 u=208 imp:p=1 imp:e=1 vol=6.745 $ sp-Vertebrae-T
209 6 -1.33 -70 u=209 imp:p=1 imp:e=1 vol=5.151 $ sp-Vertebrae-L
210 6 -1.33 -70 u=210 imp:p=1 imp:e=1 vol=2.055 $ sp-Sacrum
211 6 -1.33 -70 u=211 imp:p=1 imp:e=1 vol=5.815 $ sp-Os Coxae
212 6 -1.33 -70 u=212 imp:p=1 imp:e=1 vol=3.789 $ sp-Femora-p
213 6 -1.33 -70 u=213 imp:p=1 imp:e=1 vol=0.562 $ mc-Femora-ps
214 6 -1.33 -70 u=214 imp:p=1 imp:e=1 vol=0.898 $ mc-Femora-ds
215 6 -1.33 -70 u=215 imp:p=1 imp:e=1 vol=3.139 $ sp-Femora-d
216 6 -1.33 -70 u=216 imp:p=1 imp:e=1 vol=2.696 $ sp-Tibiae-p
217 6 -1.33 -70 u=217 imp:p=1 imp:e=1 vol=0.510 $ mc-Tibiae-s
218 6 -1.33 -70 u=218 imp:p=1 imp:e=1 vol=1.655 $ sp-Tibiae-d
219 6 -1.33 -70 u=219 imp:p=1 imp:e=1 vol=0.367 $ sp-Fibulae-p
220 6 -1.33 -70 u=220 imp:p=1 imp:e=1 vol=0.083 $ mc-Fibulae-s
221 6 -1.33 -70 u=221 imp:p=1 imp:e=1 vol=0.569 $ sp-Fibulae-d
222 6 -1.33 -70 u=222 imp:p=1 imp:e=1 vol=0.115 $ sp-Patellae
223 6 -1.33 -70 u=223 imp:p=1 imp:e=1 vol=3.201 $ sp-Ankle+Feet
224 6 -1.33 -70 u=224 imp:p=1 imp:e=1 vol=2.317 $ sp-Humera-p
225 6 -1.33 -70 u=225 imp:p=1 imp:e=1 vol=0.248 $ mc-Humera-ps
226 6 -1.33 -70 u=226 imp:p=1 imp:e=1 vol=0.248 $ mc-Humera-ds
227 6 -1.33 -70 u=227 imp:p=1 imp:e=1 vol=1.820 $ sp-Humera-d
228 6 -1.33 -70 u=228 imp:p=1 imp:e=1 vol=0.393 $ sp-Radii-p
229 6 -1.33 -70 u=229 imp:p=1 imp:e=1 vol=0.100 $ mc-Radii-s
230 6 -1.33 -70 u=230 imp:p=1 imp:e=1 vol=0.701 $ sp-Radii-d
231 6 -1.33 -70 u=231 imp:p=1 imp:e=1 vol=0.947 $ sp-Ulnae-p
232 6 -1.33 -70 u=232 imp:p=1 imp:e=1 vol=0.108 $ mc-Ulnae-s
233 6 -1.33 -70 u=233 imp:p=1 imp:e=1 vol=0.473 $ sp-Ulnae-d
234 6 -1.33 -70 u=234 imp:p=1 imp:e=1 vol=2.168 $ sp-Hands

```

c

c-----

c Window and Outside of Window

c-----

c

1002 4 -0.001205 100 -1000 imp:p=1 imp:e=1 \$ Out of Voxel, Inside medium

1003 0 1000 imp:p=0 imp:e=0 \$ Out of ROI

c

c-----

c-----

c

c Surface Card

c

c-----

c-----

c

c-----

c Phantom/Voxel/Outer Sphere Dimensions

c Phantom Array Size = ( 0:345 0:211 0:715 )

c-----

c

100 rpp 0 22.87 0 13.99 0 47.40

200 rpp 0 .0663 0 .0663 0 .0663

1000 so 200

70 so 200

c

```

c -----
c      MODE Definition
c -----
c
mode p e
c
c -----
c -----
c
c      Material Cards
c
c -----
c -----
c
c      -- Soft tissue (rho = 1.02 g/cc) --
c
M1  1000 -0.105  $ Hydrogen
    6000 -0.256  $ Carbon
    7000 -0.027  $ Nitrogen
    8000 -0.602  $ Oxygen
    11000 -0.001  $ Sodium
    15000 -0.002  $ Phosphorus
    16000 -0.003  $ Sulfur
    17000 -0.002  $ Chlorine
    19000 -0.002  $ Potassium
c
c      -- Lung (rho = 0.620) --
c
M2  1000 -0.103  $ Hydrogen
    6000 -0.105  $ Carbon
    7000 -0.031  $ Nitrogen
    8000 -0.749  $ Oxygen
    11000 -0.002  $ Sodium
    15000 -0.002  $ Phosphorus
    16000 -0.003  $ Sulfur
    17000 -0.003  $ Chlorine
    19000 -0.002  $ Potassium
c
c      -- Cortical Bone tissue (rho = 1.65) -- ICRP 89
c
M3  1000 -0.07337  $ Hydrogen
    6000 -0.25475  $ Carbon
    7000 -0.03057  $ Nitrogen
    8000 -0.47893  $ Oxygen
    9000 -0.00025  $ Fluorine
    11000 -0.00326  $ Sodium
    12000 -0.00112  $ Magnesium
    14000 -0.00002  $ Silicon
    15000 -0.05095  $ Phosphorus
    16000 -0.00173  $ Sulfur
    17000 -0.00143  $ Chlorine
    19000 -0.00153  $ Potassium
    20000 -0.10190  $ Calcium
    26000 -0.00008  $ Iron
    30000 -0.00005  $ Zinc
    37000 -0.00002  $ Rubidium

```

```

38000 -0.00003 $ Strontium
82000 -0.00001 $ Lead
c
c -- Air (rho = 0.001205) --
c
M4  6000 -0.000124 $ Carbon
    7000 -0.755267 $ Nitrogen
    8000 -0.231781 $ Oxygen
    18000 -0.012827 $ Argon
c
c -- Cartilage (rho = 1.10) -- Deanna et al.
c
M5  1000 -0.0960  $ Hydrogen
    6000 -0.0990  $ Carbon
    7000 -0.0220  $ Nitrogen
    8000 -0.7440  $ Oxygen
    11000 -0.0050  $ Sodium
    15000 -0.0220  $ Phosphorus
    16000 -0.0090  $ Sulfur
    17000 -0.0030  $ Chlorine
c
c -- Spongiosa (rho = 1.33) -- Deanna et al.
c
M6  1000 -0.0662  $ Hydrogen
    6000 -0.2357  $ Carbon
    7000 -0.0407  $ Nitrogen
    8000 -0.5003  $ Oxygen
    11000 -0.0005  $ Sodium
    12000 -0.0024  $ Magnesium
    15000 -0.0498  $ Phosphorus
    16000 -0.0027  $ Sulfur
    17000 -0.0002  $ Chlorine
    19000 -0.0003  $ Potassium
    20000 -0.1009  $ Calcium
    26000 -0.0003  $ Iron
c
c -----
c -----
c
c Tally Specification
c
c -----
c -----
c
c -----
c
c General Organ Tally (KERMA)
c -----
c
*f18:p,e  1 $ Residual Soft Tissue
*f28:p,e  2 $ Adrenal (L)
*f38:p,e  3 $ Adrenal (R)
*f48:p,e  4 $ Brain
*f58:p,e  5 $ Breast
*f68:p,e  6 $ Bronchi
*f78:p,e  7 $ Right Colon W
*f88:p,e  8 $ Right Colon C

```

\*f98:p,e 9 \$ Ears  
 \*f108:p,e 10 \$ Esophagus  
 \*f118:p,e 11 \$ External nose  
 \*f128:p,e 12 \$ Eye balls  
 \*f138:p,e 13 \$ Gall Bladder W  
 \*f148:p,e 14 \$ Gall Bladder C  
 \*f158:p,e 15 \$ Heart W  
 \*f168:p,e 16 \$ Heart C  
 \*f178:p,e 17 \$ Kidney-cortex (L)  
 \*f188:p,e 18 \$ Kidney-cortex (R)  
 \*f198:p,e 19 \$ Kidney-medulla (L)  
 \*f208:p,e 20 \$ Kidney-medulla (R)  
 \*f218:p,e 21 \$ Kidney-pelvis (L)  
 \*f228:p,e 22 \$ Kidney-pelvis (R)  
 \*f238:p,e 23 \$ Larynx  
 \*f248:p,e 24 \$ Lens  
 \*f258:p,e 25 \$ Liver  
 \*f268:p,e 26 \$ Lung (L)  
 \*f278:p,e 27 \$ Lung (R)  
 \*f288:p,e 28 \$ Nasal layer (anterior)  
 \*f298:p,e 29 \$ Nasal layer (posterior)  
 \*f308:p,e 30 \$ Oral cavity layer  
 \*f318:p,e 31 \$ Ovaries <--  
 \*f328:p,e 32 \$ Pancreas  
 c \*f338:p,e 33 \$ Penis <--  
 \*f348:p,e 34 \$ Pharynx  
 \*f358:p,e 35 \$ Pituitary Gland  
 c \*f368:p,e 36 \$ Prostate <--  
 \*f378:p,e 37 \$ Rectosigmoid W  
 \*f388:p,e 38 \$ Rectosigmoid C  
 \*f398:p,e 39 \$ Salivary Glands (parotid)  
 c \*f408:p,e 40 \$ Scrotum <--  
 \*f418:p,e 41 \$ SI W  
 \*f428:p,e 42 \$ SI C  
 \*f438:p,e 43 \$ Skin  
 \*f448:p,e 44 \$ Spinal Cord  
 \*f458:p,e 45 \$ Spleen  
 \*f468:p,e 46 \$ Stomach W  
 \*f478:p,e 47 \$ Stomach C  
 c \*f488:p,e 48 \$ Testes <--  
 \*f498:p,e 49 \$ Thymus  
 \*f508:p,e 50 \$ Thyroid  
 \*f518:p,e 51 \$ Tongue  
 \*f528:p,e 52 \$ Tonsil  
 \*f538:p,e 53 \$ Trachea  
 \*f548:p,e 54 \$ Urinary bladder W  
 \*f558:p,e 55 \$ Urinary bladder C  
 \*f568:p,e 56 \$ Uterus <--  
 \*f578:p,e 57 \$ Air (in body)  
 \*f588:p,e 58 \$ Left Colon W  
 \*f598:p,e 59 \$ Left Colon C  
 \*f608:p,e 60 \$ Salivary Glands (submaxillary)  
 \*f618:p,e 61 \$ Salivary Glands (sublingual)

c

c -----

c Cartilage Tally (KERMA)

c -----  
c  
\*f1018:p,e (101 102 103 104 105 106 107 108 109 110  
111 112 113 114 115 116 117 118 119 120  
121 122 123 124 125 126 127 128 129 130  
131)

c  
c -----  
c Spongiosa Tally (Fluence)  
c -----

c  
f2014:p 201 \$ sp-Cranium  
E2014 0.001

0.003  
0.005  
0.010  
0.015  
0.020  
0.030  
0.040  
0.050  
0.060  
0.080  
0.10  
0.15  
0.20  
0.30  
0.40  
0.50  
0.60  
0.80  
1.0  
1.5  
2.0  
3.0  
4.0  
5.0  
6.0  
8.0  
10.0

f2024:p 202 \$ sp-Mandible  
E2024 0.001

0.003  
0.005  
0.010  
0.015  
0.020  
0.030  
0.040  
0.050  
0.060  
0.080  
0.10  
0.15  
0.20  
0.30

0.40  
0.50  
0.60  
0.80  
1.0  
1.5  
2.0  
3.0  
4.0  
5.0  
6.0  
8.0  
10.0

f2034:p 203 \$ sp-Scapulae

E2034 0.001

0.003  
0.005  
0.010  
0.015  
0.020  
0.030  
0.040  
0.050  
0.060  
0.080  
0.10  
0.15  
0.20  
0.30  
0.40  
0.50  
0.60  
0.80  
1.0  
1.5  
2.0  
3.0  
4.0  
5.0  
6.0  
8.0  
10.0

f2044:p 204 \$ sp-Clavicles

E2044 0.001

0.003  
0.005  
0.010  
0.015  
0.020  
0.030  
0.040  
0.050  
0.060  
0.080  
0.10  
0.15

0.20  
0.30  
0.40  
0.50  
0.60  
0.80  
1.0  
1.5  
2.0  
3.0  
4.0  
5.0  
6.0  
8.0  
10.0

f2054;p 205 \$ sp-Sternum

E2054 0.001

0.003  
0.005  
0.010  
0.015  
0.020  
0.030  
0.040  
0.050  
0.060  
0.080  
0.10  
0.15  
0.20  
0.30  
0.40  
0.50  
0.60  
0.80  
1.0  
1.5  
2.0  
3.0  
4.0  
5.0  
6.0  
8.0  
10.0

f2064;p 206 \$ sp-Ribs

E2064 0.001

0.003  
0.005  
0.010  
0.015  
0.020  
0.030  
0.040  
0.050  
0.060  
0.080

0.10  
0.15  
0.20  
0.30  
0.40  
0.50  
0.60  
0.80  
1.0  
1.5  
2.0  
3.0  
4.0  
5.0  
6.0  
8.0  
10.0

f2074:p 207 \$ sp-Vertebrae-C

E2074 0.001

0.003  
0.005  
0.010  
0.015  
0.020  
0.030  
0.040  
0.050  
0.060  
0.080  
0.10  
0.15  
0.20  
0.30  
0.40  
0.50  
0.60  
0.80  
1.0  
1.5  
2.0  
3.0  
4.0  
5.0  
6.0  
8.0  
10.0

f2084:p 208 \$ sp-Vertebrae-T

E2084 0.001

0.003  
0.005  
0.010  
0.015  
0.020  
0.030  
0.040  
0.050

0.060  
0.080  
0.10  
0.15  
0.20  
0.30  
0.40  
0.50  
0.60  
0.80  
1.0  
1.5  
2.0  
3.0  
4.0  
5.0  
6.0  
8.0  
10.0

f2094;p 209 \$ sp-Vertebrae-L

E2094 0.001

0.003  
0.005  
0.010  
0.015  
0.020  
0.030  
0.040  
0.050  
0.060  
0.080  
0.10  
0.15  
0.20  
0.30  
0.40  
0.50  
0.60  
0.80  
1.0  
1.5  
2.0  
3.0  
4.0  
5.0  
6.0  
8.0  
10.0

f2104;p 210 \$ sp-Sacrum

E2104 0.001

0.003  
0.005  
0.010  
0.015  
0.020  
0.030

0.040  
0.050  
0.060  
0.080  
0.10  
0.15  
0.20  
0.30  
0.40  
0.40  
0.50  
0.60  
0.80  
1.0  
1.5  
2.0  
3.0  
4.0  
5.0  
6.0  
8.0  
10.0

f2114;p 211 \$ sp-Os Coxae

E2114 0.001

0.003  
0.005  
0.010  
0.015  
0.020  
0.030  
0.040  
0.040  
0.050  
0.060  
0.080  
0.10  
0.15  
0.20  
0.30  
0.40  
0.40  
0.50  
0.60  
0.80  
1.0  
1.5  
2.0  
3.0  
4.0  
5.0  
6.0  
8.0  
10.0

f2124;p 212 \$ sp-Femora-p

E2124 0.001

0.003  
0.005  
0.010  
0.015

0.020  
0.030  
0.040  
0.050  
0.060  
0.080  
0.10  
0.15  
0.20  
0.30  
0.40  
0.50  
0.60  
0.80  
1.0  
1.5  
2.0  
3.0  
4.0  
5.0  
6.0  
8.0  
10.0

f2134;p 213 \$ mc-Femora-ps

E2134 0.001

0.003  
0.005  
0.010  
0.015  
0.020  
0.030  
0.040  
0.050  
0.060  
0.080  
0.10  
0.15  
0.20  
0.30  
0.40  
0.50  
0.60  
0.80  
1.0  
1.5  
2.0  
3.0  
4.0  
5.0  
6.0  
8.0  
10.0

f2144;p 214 \$ mc-Femora-ds

E2144 0.001

0.003  
0.005

0.010  
0.015  
0.020  
0.030  
0.040  
0.050  
0.060  
0.080  
0.10  
0.15  
0.20  
0.30  
0.40  
0.50  
0.60  
0.80  
1.0  
1.5  
2.0  
3.0  
4.0  
5.0  
6.0  
8.0  
10.0

f2154:p 215 \$ sp-Femora-d  
E2154 0.001

0.003  
0.005  
0.010  
0.015  
0.020  
0.030  
0.040  
0.050  
0.060  
0.080  
0.10  
0.15  
0.20  
0.30  
0.40  
0.50  
0.60  
0.80  
1.0  
1.5  
2.0  
3.0  
4.0  
5.0  
6.0  
8.0  
10.0

f2164:p 216 \$ sp-Tibiae-p  
E2164 0.001

0.003  
0.005  
0.010  
0.015  
0.020  
0.030  
0.040  
0.050  
0.060  
0.080  
0.10  
0.15  
0.20  
0.30  
0.40  
0.50  
0.60  
0.80  
1.0  
1.5  
2.0  
3.0  
4.0  
5.0  
6.0  
8.0  
10.0

f2174:p 217 \$ mc-Tibiae-s  
E2174 0.001

0.003  
0.005  
0.010  
0.015  
0.020  
0.030  
0.040  
0.050  
0.060  
0.080  
0.10  
0.15  
0.20  
0.30  
0.40  
0.50  
0.60  
0.80  
1.0  
1.5  
2.0  
3.0  
4.0  
5.0  
6.0  
8.0  
10.0

f2184:p 218 \$ sp-Tibiae-d

E2184 0.001

0.003  
0.005  
0.010  
0.015  
0.020  
0.030  
0.040  
0.050  
0.060  
0.080  
0.10  
0.15  
0.20  
0.30  
0.40  
0.50  
0.60  
0.80  
1.0  
1.5  
2.0  
3.0  
4.0  
5.0  
6.0  
8.0  
10.0

f2194:p 219 \$ sp-Fibulae-p

E2194 0.001

0.003  
0.005  
0.010  
0.015  
0.020  
0.030  
0.040  
0.050  
0.060  
0.080  
0.10  
0.15  
0.20  
0.30  
0.40  
0.50  
0.60  
0.80  
1.0  
1.5  
2.0  
3.0  
4.0  
5.0  
6.0

8.0  
10.0  
f2204:p 220 \$ mc-Fibulae-s  
E2204 0.001

0.003  
0.005  
0.010  
0.015  
0.020  
0.030  
0.040  
0.050  
0.060  
0.080  
0.10  
0.15  
0.20  
0.30  
0.40  
0.50  
0.60  
0.80  
1.0  
1.5  
2.0  
3.0  
4.0  
5.0  
6.0  
8.0  
10.0

f2214:p 221 \$ sp-Fibulae-d  
E2214 0.001

0.003  
0.005  
0.010  
0.015  
0.020  
0.030  
0.040  
0.050  
0.060  
0.080  
0.10  
0.15  
0.20  
0.30  
0.40  
0.50  
0.60  
0.80  
1.0  
1.5  
2.0  
3.0  
4.0

5.0  
6.0  
8.0  
10.0  
f2224:p 222 \$ sp-Patellae  
E2224 0.001  
0.003  
0.005  
0.010  
0.015  
0.020  
0.030  
0.040  
0.050  
0.060  
0.080  
0.10  
0.15  
0.20  
0.30  
0.40  
0.50  
0.60  
0.80  
1.0  
1.5  
2.0  
3.0  
4.0  
5.0  
6.0  
8.0  
10.0  
f2234:p 223 \$ sp-Ankle+Feet  
E2234 0.001  
0.003  
0.005  
0.010  
0.015  
0.020  
0.030  
0.040  
0.050  
0.060  
0.080  
0.10  
0.15  
0.20  
0.30  
0.40  
0.50  
0.60  
0.80  
1.0  
1.5  
2.0

3.0  
4.0  
5.0  
6.0  
8.0  
10.0

f2244:p 224 \$ sp-Humera-p  
E2244 0.001

0.003  
0.005  
0.010  
0.015  
0.020  
0.030  
0.040  
0.050  
0.060  
0.080  
0.10  
0.15  
0.20  
0.30  
0.40  
0.50  
0.60  
0.80  
1.0  
1.5  
2.0  
3.0  
4.0  
5.0  
6.0  
8.0  
10.0

f2254:p 225 \$ mc-Humera-ps  
E2254 0.001

0.003  
0.005  
0.010  
0.015  
0.020  
0.030  
0.040  
0.050  
0.060  
0.080  
0.10  
0.15  
0.20  
0.30  
0.40  
0.50  
0.60  
0.80  
1.0

1.5  
2.0  
3.0  
4.0  
5.0  
6.0  
8.0  
10.0

f2264;p 226 \$ mc-Humera-ds

E2264 0.001

0.003  
0.005  
0.010  
0.015  
0.020  
0.030  
0.040  
0.050  
0.060  
0.080  
0.10  
0.15  
0.20  
0.30  
0.40  
0.50  
0.60  
0.80  
1.0  
1.5  
2.0  
3.0  
4.0  
5.0  
6.0  
8.0  
10.0

f2274;p 227 \$ sp-Humera-d

E2274 0.001

0.003  
0.005  
0.010  
0.015  
0.020  
0.030  
0.040  
0.050  
0.060  
0.080  
0.10  
0.15  
0.20  
0.30  
0.40  
0.50  
0.60

0.80  
1.0  
1.5  
2.0  
3.0  
4.0  
5.0  
6.0  
8.0  
10.0

f2284:p 228 \$ sp-Radii-p

E2284 0.001

0.003  
0.005  
0.010  
0.015  
0.020  
0.030  
0.040  
0.050  
0.060  
0.080  
0.10  
0.15  
0.20  
0.30  
0.40  
0.50  
0.60  
0.80  
1.0  
1.5  
2.0  
3.0  
4.0  
5.0  
6.0  
8.0  
10.0

f2294:p 229 \$ mc-Radii-s

E2294 0.001

0.003  
0.005  
0.010  
0.015  
0.020  
0.030  
0.040  
0.050  
0.060  
0.080  
0.10  
0.15  
0.20  
0.30  
0.40

0.50  
0.60  
0.80  
1.0  
1.5  
2.0  
3.0  
4.0  
5.0  
6.0  
8.0  
10.0

f2304:p 230 \$ sp-Radii-d

E2304 0.001

0.003  
0.005  
0.010  
0.015  
0.020  
0.030  
0.040  
0.050  
0.060  
0.080  
0.10  
0.15  
0.20  
0.30  
0.40  
0.50  
0.60  
0.80  
1.0  
1.5  
2.0  
3.0  
4.0  
5.0  
6.0  
8.0  
10.0

f2314:p 231 \$ sp-Ulnae-p

E2314 0.001

0.003  
0.005  
0.010  
0.015  
0.020  
0.030  
0.040  
0.050  
0.060  
0.080  
0.10  
0.15  
0.20

0.30  
0.40  
0.50  
0.60  
0.80  
1.0  
1.5  
2.0  
3.0  
4.0  
5.0  
6.0  
8.0  
10.0

f2324:p 232 \$ mc-Ulnae-s  
E2324 0.001

0.003  
0.005  
0.010  
0.015  
0.020  
0.030  
0.040  
0.050  
0.060  
0.080  
0.10  
0.15  
0.20  
0.30  
0.40  
0.50  
0.60  
0.80  
1.0  
1.5  
2.0  
3.0  
4.0  
5.0  
6.0  
8.0  
10.0

f2334:p 233 \$ sp-Ulnae-d  
E2334 0.001

0.003  
0.005  
0.010  
0.015  
0.020  
0.030  
0.040  
0.050  
0.060  
0.080  
0.10

```

0.15
0.20
0.30
0.40
0.50
0.60
0.80
1.0
1.5
2.0
3.0
4.0
5.0
6.0
8.0
10.0
f2344:p 234 $ sp-Hands
E2344 0.001
0.003
0.005
0.010
0.015
0.020
0.030
0.040
0.050
0.060
0.080
0.10
0.15
0.20
0.30
0.40
0.50
0.60
0.80
1.0
1.5
2.0
3.0
4.0
5.0
6.0
8.0
10.0
c
c -----
c -----
c
c      Source Definition
c
c -----
c -----
c
sdef par=p erg=4.0000 cel=d5 x=d1 y=d2 z=d3
read file=liver.src noecho

```

```
# si1 sp1 si2 sp2 si3 sp3
0 0 0 0 0 0
.0663 1 .0663 1 .0663 1
nps 1e7
```

APPENDIX B  
ORIGINAL CODES

**Skeletal Dose Response Function Code**

```
tic

drf_am=xlsread('drf.xls','am','b4:u31');
drf_am50=xlsread('drf.xls','am50','b4:u31');

massf_am=xlsread('AM and AM50 Mass Fractions.xls','am','g1:g20');
massf_am50=xlsread('AM and AM50 Mass Fractions.xls','am50','m1:m20');

[arb1,sourcematrix] = xlsread('nb voxel count.xls','MATLABf');
[arb2,safcellnums] = xlsread('saf indices.xls','Sheet1');
energyindex = xlsread('saf indices.xls','Sheet1','e1:e1281');
sourceindex = xlsread('saf indices.xls','Sheet1','f1:f1281');
sourceabbrev = sourcematrix(:,3);

fid_o_read = fopen('outputfilenames','r');
datafiles = textscan(fid_o_read,'%s','delimiter','\n');

for outputnum=1:61*21

% Cycling through each output filename
outputname = datafiles{1}{outputnum}
fid = fopen(outputname,'r');

% Reading text in from output file
inputtext = textscan(fid,'%s','delimiter','\n');
lines = length(inputtext{1});
placeholder=0;
bonesite=0;
format long e;

% Reading in ENERGY -----

for i=1:lines

energyflag = findstr('1390- sdef',inputtext{1}{i});

if energyflag == 1

energy = textscan(inputtext{1}{i},'%*27c%n%*s%*s%*s%*s');
break

end

end

% -----
```

```

for i=1:lines
    placeholder=placeholder+1;
    % Finding beginning of energy dependent fluences
    drfflag = findstr('cell 201',inputtext{1}{i});

    if drfflag == 1
        break
    end

end

% Reading in energy dependent fluences for every bone site
for i=placeholder:lines

    drfflag2 = findstr('cell ',inputtext{1}{i});

    if drfflag2 == 1
        bonesite=bonesite+1;
        for j=1:28
            fluence_temp(j,bonesite)=textscan(inputtext{1}{i+1+j}, '%*n%n%*n');
        end
    end

    if bonesite == 34
        break
    end

end

% Multiplying the drf by the fluence at each energy
for i=1:20
    for j=1:28
        drf_am_fluence{j,i}=fluence{j,i}.*drf_am(j,i).*massf_am(i);
        drf_am50_fluence{j,i}=fluence{j,i}.*drf_am50(j,i).*massf_am50(i);
    end
end

% Calculating the whole skeleton SAF for AM and AM50
SAF_am=(6.24142e+13/energy{1})*sum(sum(cell2mat(drf_am_fluence)));
SAF_am50=(6.24142e+13/energy{1})*sum(sum(cell2mat(drf_am50_fluence)));

xlswrite('Newborn SAFs female - photons
test',SAF_am,sourceabbrev{sourceindex(outputnum)},safcellnums{energyindex(out
putnum),7});
xlswrite('Newborn SAFs female - photons
test',SAF_am50,sourceabbrev{sourceindex(outputnum)},safcellnums{energyindex(o
utputnum),8});

end

fclose('all');

toc/60

```

## MCNPX Output File Post-processing Code

```
energy = xlsread('nb voxel count.xls', 'MATLABf', 'd1:d21');
[arb1, sourcematrix] = xlsread('nb voxel count.xls', 'MATLABf');
[arb2, safcellnums] = xlsread('saf indices.xls', 'Sheet1');
energyindex = xlsread('saf indices.xls', 'Sheet1', 'e1:e1281');
sourceindex = xlsread('saf indices.xls', 'Sheet1', 'f1:f1281');

sourceabbrev = sourcematrix(:,3);
outputfilenames = sprintf('outputfilenames');
fid_o = fopen(outputfilenames, 'wt');

% Creating a file that lists all the output filenames in one column
for i=1:length(sourceabbrev)
    for j=1:length(energy)
        fprintf(fid_o, '%s%0.0f%s\n', char(sourceabbrev(i)), char(j), 'fp.o');
    end
end

fclose(fid_o);

fid_o_read = fopen('outputfilenames', 'r');
datafiles = textscan(fid_o_read, '%s', 'delimiter', '\n');

[arb3, cellnumber] = xlsread('Misc Output Info test.xls', 'Cell Numbers - f');

index=0;
for i=1:61
    for j=1:21
        index=index+1;
        cellnum(index)=cellnumber(i,j);
    end
end

for outputnum=1:61*21

% Cycling through each output filename
outputname = datafiles{1}{outputnum}
fid = fopen(outputname, 'r');

% Reading text in from output file
inputtext = textscan(fid, '%s', 'delimiter', '\n');

count6 = 0;
count8 = 0;
count4 = 0;
counte = 0;
format short e;
lines = length(inputtext{1});

% Reading in COMPUTER TIME -----

for i=1:lines
```

```

timeflag = findstr('computer time =',inputtext{1}{i});

if timeflag == 1

    comptime = textscan(inputtext{1}{i},'%*16c%n%*s');
    break

end
end

xlswrite('Misc Output Info test.xls',comptime,'Computer Time -
f',cellnum{outputnum});

% -----

% Reading in ENERGY -----

for i=1:lines

    energyflag = findstr('1390-      sdef',inputtext{1}{i});

    if energyflag == 1

        energy = textscan(inputtext{1}{i},'%*27c%n%*s%*s%*s%*s');
        break

    end

end

% -----

% MASS PROCESSING -----

% Reading in organ masses
for i=1:lines

    massflag = findstr('3      1',inputtext{1}{i});

    if massflag == 1

        for j=1:156
            organmass(j) = textscan(inputtext{1}{i+j-
1},'%*n%*n%*n%*n%*n%*n%*n%*n%*n');
            end

            break

        end

end
end

```

```

end

% General organ masses
for i=1:57
    genorganmass(i) = organmass(i);
end

% Total cartilage mass
cartmass = 0;
for i=1:31
    cartmass = cartmass + organmass{57+i};
end
% -----

% TALLY PROCESSING -----

% Reading in the tally values (F6,*F8,F4) and ERRORS from output file
for i=1:lines

    % Determining if it is an F6 or a *F8 tally ('mode p e' --> F8)
    tallytypeflag = findstr('220-      mode p e',inputtext{1}{i});

    if tallytypeflag == 1
        break
    end

end

% If this is a *F8 tally
if tallytypeflag == 1

    % Reading through each line of the output file
    for i=1:lines

        % Finding the start of the tally values
        targetflag = findstr('1000000',inputtext{1}{i});

        % Reading in the tally values from the each line deemed a tally
value line
        if targetflag == 1

            count8 = count8+1;
            tally8_3column(count8,:) =
textscan(inputtext{1}{i}, '%*n%n%n%n%n%n%n%n%n%n%n%n%n%n%n%n%n%n');
            error_3column(count8,:) =
textscan(inputtext{1}{i}, '%*n%n%n%n%n%n%n%n%n%n%n%n%n%n%n%n%n');

            end
        end
    end
end

```

```

numtallies = 0;

% Creating a one dimensional array of tallies from a two dimensional
array
for i=1:count8
    for j=1:3
        numtallies = numtallies+1;
        tally8temp(numtallies) = tally8_3column(i,j);
        errortemp(numtallies) = error_3column(i,j);
    end
end

% Deleting the last entry (tally6_3column(count6,3) = 0)
for i=1:count8*3-1
    tally8(i) = tally8temp(i);
    error8(i) = errortemp(i);
end

for j=1:57
    SAF8{j} = tally8{j+34}/(genorganmass{j}*energy{1});
    error(j)=error8(j+34);
end

carterr=error8(58+34);
cartSAF=tally8{58+34}/cartmass;

xlswrite('Newborn SAFs female - photons
test',SAF8(:),sourceabbrev{sourceindex(outputnum)},safcellnums{energyindex(ou
tputnum),1});
xlswrite('Newborn SAFs female - photons
test',cartSAF,sourceabbrev{sourceindex(outputnum)},safcellnums{energyindex(ou
tputnum),2});
xlswrite('Newborn SAFs female - photons
test',SAF8(:),sourceabbrev{sourceindex(outputnum)},safcellnums{energyindex(ou
tputnum)-9,3});
xlswrite('Newborn SAFs female - photons
test',cartSAF,sourceabbrev{sourceindex(outputnum)},safcellnums{energyindex(ou
tputnum)-9,4});
xlswrite('Newborn SAFs female - photons (error)
test',error(:),sourceabbrev{sourceindex(outputnum)},safcellnums{energyindex(o
utputnum),1});
xlswrite('Newborn SAFs female - photons (error)
test',carterr,sourceabbrev{sourceindex(outputnum)},safcellnums{energyindex(ou
tputnum),2});
xlswrite('Newborn SAFs female - photons (error)
test',error(:),sourceabbrev{sourceindex(outputnum)},safcellnums{energyindex(o
utputnum)-9,3});
xlswrite('Newborn SAFs female - photons (error)
test',carterr,sourceabbrev{sourceindex(outputnum)},safcellnums{energyindex(ou
tputnum)-9,4});

% If this is an F6 tally
else

```

```

% Reading through each line of the output file
for i=1:lines

    % Finding the start of the tally values
    targetflag = findstr('100000000',inputtext{1}{i});

    % Reading in the tally values from the each line deemed a tally
value line
    if targetflag == 1

        count6 = count6+1;
        tally6_3column(count6,:) =
textscan(inputtext{1}{i}, '%*n%n%n*n%n%n*n%n*n%n*n%n*n*n*n');
        error_3column(count6,:) =
textscan(inputtext{1}{i}, '%*n*n%n*n*n*n*n*n*n*n*n*n*n*n*n*n');

        end

    end

numtallies = 0;

% Creating a one dimensional array of tallies from a two dimensional
array
for i=1:count6
    for j=1:3
        numtallies = numtallies+1;
        tally6temp(numtallies) = tally6_3column(i,j);
        error6temp(numtallies) = error_3column(i,j);
    end
end

% Deleting the last entry (tally6_3column(count6,3) = 0)
for i=1:count6*3-1
    tally6(i) = tally6temp(i);
    error6(i) = error6temp(i);
end

for j=1:57
    SAF6{j} = tally6{j}/energy{1};
    error(j)=error6(j);
end

carterr=error6(58);
cartSAF=tally6{58}/cartmass;

xlswrite('Newborn SAFs female - photons
test',SAF6(:),sourceabbrev{sourceindex(outputnum)},safcellnums{energyindex(ou
tputnum),1});
xlswrite('Newborn SAFs female - photons
test',cartSAF,sourceabbrev{sourceindex(outputnum)},safcellnums{energyindex(ou
tputnum),2});
xlswrite('Newborn SAFs female - photons (error)
test',error(:),sourceabbrev{sourceindex(outputnum)},safcellnums{energyindex(o
utputnum),1});

```

```
        xlswrite('Newborn SAFs female - photons (error)
test', carterr, sourceabbrev{sourceindex(outputnum)}, safcellnums{energyindex(ou
tputnum), 2});

end

fclose('all');

end
```

## LIST OF REFERENCES

1. American College of Radiology. *Image Gently Campaign Named to Associations Advance America Honor Roll*. 2009.  
<http://www.acr.org/SecondaryMainMenuCategories/NewsPublications/FeaturedCategories/CurrentACRNews/archive/ImageGentlyCampaignHonorRoll.aspx>. Accessed 9/09.
2. The Alliance for Radiation Safety in Pediatric Imaging. *Image gently...Step Lightly*.  
<http://spr.affiniscape.com/associations/5364/ig/index.cfm?page=584>. Accessed 9/09.
3. Harrison JD, Streffer C. The ICRP protection quantities, equivalent and effective dose: their basis and application. *Radiat Prot Dosim*. 2007;127:12-18.
4. Hall EJ, Giaccia AJ. *Radiobiology for the Radiologist, Sixth Edition*. Philadelphia, PA: Lippincott Williams & Wilkins; 2006.
5. Brownell GL, Ellett WH, Reddy AR. MIRD pamphlet no. 3: absorbed fractions for photon dosimetry. *J Nucl Med*. 1968;9(suppl):27-39.
6. National Council on Radiation Protection and Measurements (NCRP). *Protection Against Neutron Radiation*. Report No. 38. Bethesda, MD: NCRP; 1971.
7. Snyder WS, Ford MR, Warner GG, et al. MIRD pamphlet no. 5: estimates of absorbed fractions for monoenergetic photon sources uniformly distributed in various organs of a heterogeneous phantom. *J Nucl Med*. 1969;10(suppl):5-52.
8. Snyder WS, Ford MR, Warner GG, et al. MIRD pamphlet no. 5, revised: estimates of absorbed fractions for monoenergetic photon sources uniformly distributed in various organs of a heterogeneous phantom. *J Nucl Med*. 1978;10(suppl):5-67.
9. Cristy M, Eckerman KF. *Specific Absorbed Fractions of Energy at Various Ages from Internal Photon Sources. I. Methods*. ORNL/TM-8381/V1. Oak Ridge, TN: Oak Ridge National Laboratories; 1987.
10. Xu XG, Chao TC, Bozkurt A. VIP-man: an image-based whole-body adult male model constructed from color photographs of the Visible Human Project for multi-particle Monte Carlo calculations. *Health Phys*. 2000;78:476-486.
11. Petoussi-Hens N, Zankl M, Fill U, Regulla D. The GSF family of voxel phantoms. *Phys Med Biol*. 2002;47:89-106.
12. Lee C, Lodwick D, Hasenauer D, Williams JL, Lee C, Bolch WE. Hybrid computational phantoms of the male and female newborn patient: NURBS-based whole-body models. *Phys Med Biol*. 2007;52:3309-3333.
13. Nipper JC, Williams JL, Bolch WE. Creation of two tomographic voxel models of paediatric patients in the first year of life. *Phys Med Biol*. 2002;47:3143-3164.

14. Pafundi D, Lee C, Watchman C, et al. An image-based skeletal tissue model for the ICRP reference newborn. *Phys Med Biol.* 2009;54:4497-4531.
15. Rajon DA, Pichardo JC, Brindle JM, et al. Image segmentation of trabecular spongiosa by visual inspection of the gradient magnitude. *Phys Med Biol.* 2006;51:4447-4467.
16. Pafundi D, Rajon D, Jokisch D, Lee C, Bolch WE. An image-based skeletal dosimetry model for the ICRP reference newborn – internal electron sources. *Phys Med Biol.* In press.
17. X-5 Monte Carlo Team. *MCNP – A General Monte Carlo N-Particle Transport Code, Version 5.* LA-UR-03-1987. Los Alamos National Laboratories; 2003.
18. International Commission on Radiological Protection (ICRP). *Basic Anatomical and Physiological Data for Use in Radiological Protection: Reference Values.* ICRP Publication 89. Oxford, U.K.: Pergamon Press; 2002.
19. Bolch WE, Eckerman KF, Sgouros G, Thomas SR. MIRD pamphlet no. 21: a generalized schema for radiopharmaceutical dosimetry - standardization of nomenclature. *J Nucl Med.* 2009;50:477-484.
20. Treves ST. *Pediatric Nuclear Medicine, Second Edition.* New York, NY: Springer-Verlag New York Inc.; 1995.
21. Arnold RW, Subramanian G, McAfee JG, Blair RJ, Thomas FD. Comparison of tc-99m complexes for renal imaging. *J Nucl Med.* 1975;16:357-367.
22. Evans E, Lythgoe MF, Anderson PJ, Smith Terry, Gordon I. Biokinetic behavior of technetium-99m-DMSA in children. *J Nucl Med.* 1996;37:1331-1335.
23. Smith T, Evans K, Lythgoe MF, Anderson PJ, Gordon I. Radiation dosimetry of technetium-99m-DMSA in children. *J Nucl Med.* 1996;37:1336-1342.
24. Faw RE, Shultis JK. *Radiological Assessment: Sources and Doses.* La Grange Park, IL: American Nuclear Society, Inc.; 1999.
25. International Commission on Radiological Protection (ICRP). 2007 Recommendations of the International Commission on Radiological Protection. ICRP Publication 103. *Ann ICRP.* 2007;37:1-332.
26. Cherry SR, Sorenson JA, Phelps ME. *Physics in Nuclear Medicine, Third Edition.* Philadelphia, PA: Saunders; 2003.
27. Cristy M, Eckerman KF. *Specific Absorbed Fractions of Energy at Various Ages from Internal Photon Sources. VI. Newborn.* ORNL/TM-8381/V6. Oak Ridge, TN: Oak Ridge National Laboratories; 1987.

28. Treves ST, Davis RT, Fahey FH. Administered radiopharmaceutical doses in children: a survey of 13 pediatric hospitals in North America. *J Nucl Med.* 2008;49:1024-1027.

## BIOGRAPHICAL SKETCH

Michael Brice Wayson was born in 1986 in Orlando, Florida to Mark and Niki Wayson. He has two younger brothers, Brant and Zachary. He has spent most of his life living in Brandon, FL, which is just outside Tampa, FL, but has also resided in Orlando, FL, West Palm Beach, FL, and Richmond, VA. He graduated from Bloomingdale Senior High School in the spring of 2004. He graduated *cum laude* with his B.S. in nuclear engineering at the University of Florida in December 2007 and is in the process of completing his M.S. in nuclear engineering Sciences with a specialty in Medical Physics at the University of Florida. He plans to earn a Ph.D. in Medical Physics at the University of Florida upon completion of the M.S. degree.

Michael has a wide variety of extracurricular interests. He participates extensively in sporting events including football and basketball intramural competitions. He has played organized baseball, basketball, golf, track, cross country, and football throughout his life. He enjoys traveling and has been to 21 of the 50 United States in addition to Jamaica, the Cayman Islands, Canada, and Italy. He especially enjoys snow skiing and has been skiing at Copper Mountain, CO, Big Sky/Moonlight Basin, MT, and Whistler Mountain, BC, Canada. Another hobby Michael enjoys is piano performance and music composition.

He was recently engaged to Ms. Leslie Ann Hooker who has continued to support him in his endeavor to complete his Master of Science and Doctor of Philosophy degrees. She is whom this master's thesis and any subsequent works are ultimately for.